Earth-Science Reviews 246 (2023) 104576

Contents lists available at ScienceDirect

Earth-Science Reviews

journal homepage: www.elsevier.com/locate/earscirev

Dynamics of Tethyan marine de-oxygenation and relationship to S-N-P cycles during the Permian-Triassic boundary crisis

Yuzhu Ge [a,b,*], Thomas J. Algeo [c,d,e,**], Huaguo Wen [a,b], Chen Zhang [a,b], Yiquan Ma [a,b], Chengbo Lian [f]

[a] State Key Laboratory of Oil and Gas Reservoir Geology and Exploitation, Chengdu University of Technology, Chengdu 610059, China
[b] Institute of Sedimentary Geology & Key Laboratory of Deep-time Geography & Environmental Reconstruction and Application of Ministry of Natural Resources, Chengdu University of Technology, Chengdu 610059, China
[c] State Key Laboratory of Biology and Environmental Geology, China University of Geoscience, Wuhan, Hubei 430074, China
[d] State Key Laboratory of Geological Processes and Mineral Resources, China University of Geosciences, Wuhan, Hubei 430074, China
[e] Department of Geosciences, University of Cincinnati, Cincinnati, OH 45221-0013, USA
[f] School of Geoscience and Technology, Southwest Petroleum University, Chengdu 610500, China

ARTICLE INFO

Keywords:
Tethys
Ocean redox
Volcanism
Biocrisis
Mass extinction

ABSTRACT

Oceanic de-oxygenation is considered to have been an important kill mechanism contributing to the latest Permian mass extinction and subsequent protracted recovery of marine biotas, but its extent, magnitude, and related controlling factors remain controversial. Here, we undertake a synthesis and reevaluation of previously published Fe-S-P-N data to better understand spatial and temporal variation of marine de-oxygenation along a proximal-to-distal gradient in the eastern Paleotethys Ocean during the Permian-Triassic transition. Our results indicate: i) transient oxygenation of outer-shelf to basinal settings and de-oxygenation of middle-shelf settings at the extinction horizon; ii) in outer-shelf to basinal settings, a shift from episodically euxinic conditions in the latest Permian (*C. changxingensis* Zone) to mainly ferruginous conditions in the earliest Triassic (*H. parvus-I. isarcica* zones); and iii) in middle-shelf settings, a shift from oxic-dysoxic (*C. changxingensis* Zone) to euxinic (*C. yini-C. meishanensis* zones) and then back to oxic conditions (*H. parvus-I. isarcica* zones). Proximal-to-distal redox variations are closely linked to spatial gradients in the marine sulfur, nitrogen and phosphorous cycles. A global comparison demonstrates that the Paleotethys, Neotethys, Boreal, and Panthalassic oceans all experienced shallow-marine de-oxygenation during the latest Permian mass extinction, which may have been a major factor in the marine biocrisis. Globally, the extent and magnitude of oceanic de-oxygenation presented a link to the distance to the Siberian Traps Large Igneous Province and, thus, to the volume of volcanic-related sulfur release during the Permian-Triassic boundary crisis.

1. Introduction

Marine redox and nutrient conditions, and their spatial characterization highly affect life evolution processes, such as mass extinction and subsequent recovery (e.g., Grasby et al., 2013; Schobben et al., 2020; Müller et al., 2022). One prominent case is the Permian-Triassic mass extinction event. The Permian-Triassic (P-Tr) transition experienced the largest biocrisis of the Phanerozoic, i.e., the latest Permian mass extinction (LPME; ca. 252 Ma), followed by a protracted (~5 Myr) and complex period of marine ecosystem recovery during the Early Triassic (Pietsch and Bottjer, 2014; Brayard et al., 2017; Song et al., 2018). Both terrestrial and marine biotas suffered severe losses linked to major environmental changes (Jin et al., 2000; Smith and Ward, 2001; Song et al., 2013b). The biotic crisis and underlying environmental perturbations are generally regarded as having been triggered by massive eruptions of the Siberian Traps Large Igneous Province (STLIP; e.g., Renne et al., 1995; Kamo et al., 2003; Reichow et al., 2009; Chen et al., 2014).

Expansion of oceanic anoxia is one of the most frequently proposed kill mechanisms for the marine mass extinction, and it is thought to have strongly influenced the habitability of marine environments during the P-Tr transition (Wignall and Twitchett, 1996; Isozaki, 1997; Erwin et al.,

* Correspondence to: Y. Ge, State Key Laboratory of Oil and Gas Reservoir Geology and Exploitation, Chengdu University of Technology, Chengdu 610059, China.
** Correspondence to: T. J. Algeo, State Key Laboratory of Biology and Environmental Geology, China University of Geoscience, Wuhan, Hubei 430074, China.
E-mail addresses: geyuzhu2021@cdut.edu.cn (Y. Ge), thomas.algeo@uc.edu (T.J. Algeo).

https://doi.org/10.1016/j.earscirev.2023.104576
Received 8 March 2023; Received in revised form 18 August 2023; Accepted 26 September 2023
Available online 28 September 2023

2002; Grasby et al., 2013; Zhang et al., 2020). Many studies have examined redox conditions in limited regions of the P-Tr global ocean (e.g., Grice et al., 2005; Algeo et al., 2007, 2011; Bond and Wignall, 2010; Wei et al., 2015; Clarkson et al., 2016; Schobben et al., 2020; Saitoh et al., 2021), and a few studies have examined average global ocean-redox changes based on redox-sensitive isotopic proxies with long seawater residence times (e.g., Lau et al., 2016; Zhang et al., 2018a, 2020; Newby et al., 2021). However, no study to date has taken a holistic view of redox changes in multiple regions of the P-Tr global ocean to try to understand the nature of forcings and the evolutionary history of watermass redox changes. Moreover, oceanic anoxia can involve either ferruginous (Fe^{2+} rich) or euxinic (H_2S rich) waters, the distribution of which in the P-Tr global ocean is not well-constrained, yet is critical for understanding seawater chemistry (e.g., $[SO_4]_{sw}$) and bio-nutrient cycles (e.g., Fe, N, P) (Clarkson et al., 2016; Schobben et al., 2020; Müller et al., 2022).

Analysis of proximal-to-distal transects across shelf-slope-basin environments are a key method of reconstructing watermass redox characteristics in marine depositional systems. This whole water-column approach to redox analysis has been utilized in P-Tr studies of the Arabian Margin in the Neotethys Ocean (Clarkson et al., 2016) and the Boreal Sea shelf on the northern Pangean margin (Schobben et al., 2020). Shallow-to-deep redox characteristics have also been reconstructed from different components of deep-ocean sediments, as for the central Panthalassic Ocean (Isozaki, 1997; Suzuki et al., 1998; Kato et al., 2002; Matsuo et al., 2003; Algeo et al., 2010, 2011).

These studies have inferred markedly different water-column redox structures, leading to development of multiple ocean geochemical models for the P-Tr transition (e.g., Li et al., 2016; Xiang et al., 2020; Wu et al., 2022). A similar proximal-to-distal investigation of watermass redox characteristics is lacking for the Paleotethys, where many P-Tr sections from both shallow and deep settings have been studied independently (e.g., Riccardi et al., 2006; Li et al., 2016; Lei et al., 2017; Xiang et al., 2020) but no model making use of regionally integrated data has been proposed to date.

Focusing on the P-Tr transition interval (*C. wangi* to *I. isarcica* conodont zones), the goals of the present study are: (1) to reconstruct the history of shallow-to-deep redox evolution of the Paleotethys Ocean based on numerous sections from South China; (2) to assess coupling between marine redox evolution and S-N-P cycling in an integrated environmental model for the Paleotethys; and (3) to compare our results for the Paleotethys with equivalent data for the Neotethys, Panthalassic, and Boreal oceans to achieve holistic insights into global-ocean redox evolution during this critical interval of Earth history. Our reconstruction will make use of 11 well-studied P-Tr sections in South China spanning a shelf-to-basin transect (Fig. 1). Redox conditions will be evaluated using a combination of previously published mineralogic and geochemical data, including Fe-speciation, framboidal pyrite size distributions, S-isotopes of pyrite ($\delta^{34}S_{pyrite}$) and carbonate-associated sulfur ($\delta^{34}S_{CAS}$), TOC/P, and $\delta^{15}N_{org}$. Here, we assemble existing data for specific water-depth ranges (shallow or deep) from previous P-Tr studies to build a dataset representing a shallow-to-deep transect. Based on a larger proxy dataset than used in earlier studies, we evaluate it systematically to better understand the extent and magnitude of marine de-oxygenation during the P-Tr transition.

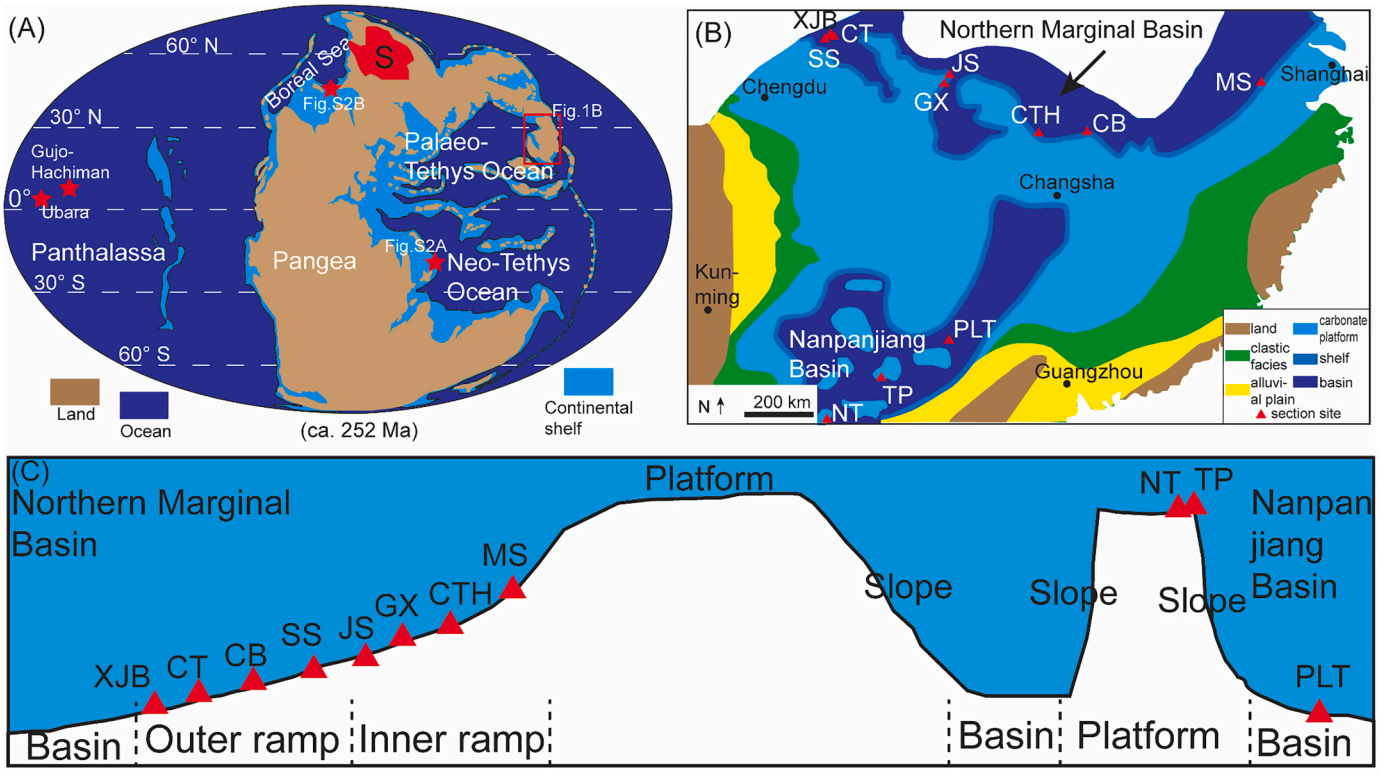

Fig. 1. (A) Global paleogeography. The South China Craton is indicated by the red frame. The comparison sites (Neotethys, Boreal Sea, Panthalassa) are indicated by red stars. Detailed study sections in Neotethys and Boreal Sea can be seen in Fig. S2. The red polygon with S is the Siberian Traps Large Igneous Province. Modified from Algeo et al. (2010, 2011), Clarkson et al. (2016), Xiao et al. (2018) and Schobben et al. (2020). (B) South China paleogeography. The sections in this study are indicated by red triangles. Modified from Yin et al. (2014). (C) Transect from shallow-water carbonate platform to basinal settings, showing the locations of study sections. Relative water depths were based on Algeo et al. (2007, 2008), He et al. (2013), Wei et al. (2015), Xiao et al. (2018), Müller et al. (2022), and Wu et al. (2022). Abbreviations: CB–Chibi, CT–Chaotian, CTH–Changtahe, GX–Ganxi, JS–Jianshi, MS–Meishan, NT–Nhi Tao, PLT–Penglaitan, SS–Shangsi, TP–Taiping, and XJB–Xiaojiaba. (For interpretation of the references to colour in this figure legend, the reader is referred to the web version of this article.)

2. Geological setting

During the P-Tr transition, the South China Craton was located at a low paleolatitude (~15–30°N) in the eastern Paleotethys Ocean (Scotese and Langford, 1995) (Fig. 1A). The shallow-marine Yangtze Platform developed on the center of this craton, surrounded by the Kangdian Oldland to the west, the deep-water Nanpanjiang (or Hunan-Guizhou-Guangxi) Basin to the south, the Cathaysian and Yunkai oldlands to the east, and the deep-water Northern Marginal Basin to the north (Wang and Jin, 2000; Yin et al., 2014) (Fig. 1B). In South China, many continuous marine P-Tr sections have been investigated, providing a large amount of data about redox conditions (e.g., Li et al., 2016; Xiang et al., 2020) and S-N-P cycles (e.g., Riccardi et al., 2006; Algeo et al., 2007; Luo et al., 2011; Xiang et al., 2016; Müller et al., 2022; Wu et al., 2022).

The P-Tr sections utilized in this study represent mainly carbonate ramp to basinal settings in the northern part and carbonate platform to basinal settings in the southern part of the South China Craton (Fig. 1C). They span a range of depositional water depths, which have been assessed previously based on sedimentary structures and biota (Lei et al., 2012; Song et al., 2013b; Shen et al., 2015; Xiao et al., 2018). Basic geological information (e.g., lithology, water depth) and previous redox-related studies of these sections are summarized in Table 1 (Lei et al., 2012; Song et al., 2013a; Shen et al., 2015; Xiao et al., 2017; Ge and Bond, 2022). In order to conduct a proximal-to-distal analysis, the study sections were assigned to one of three water-depth ranges based on sedimentological and biotic features and paleowater depth evaluations in previous work (Lei et al., 2012; Song et al., 2013a; Shen et al., 2015; Xiao et al., 2018) (Table 1): (i) inner-shelf (Nhi Tao, Taiping), including carbonate platform top and interior facies characterized by fossiliferous limestone with diverse benthic metazoan fossil in the uppermost Permian, and by microbialites and/or oolitic limestone in the lowermost Triassic; (ii) middle-shelf (Meishan, Changtahe, Ganxi, Jianshi), including upper carbonate ramp settings characterized by fossiliferous limestone with diverse benthic metazoan fossils in the uppermost Permian, and by mainly micritic or muddy limestone in the lowermost Triassic; and (iii) outer-shelf to basin (Shangsi, Chibi, Chaotian, Xiaojiaba, Penglaitan), including lower carbonate ramp or slope to basinal facies characterized by cherty sediment enriched in radiolarians and ammonites in the uppermost Permian, and by mainly micritic or muddy limestone in the lowermost Triassic. Then, for each water-depth range, multiple redox and nutrient geochemical proxies (e.g., Fe species, pyrites, $\delta^{34}S$, TOC/P, $\delta^{15}N$, P) were collected from multiple sections in order to better evaluate marine redox and nutrient conditions from different aspects. One assumption is that similar characteristics of the same geochemical record from different sections can reasonably be used to discuss relevant changes of marine conditions in each water-depth range.

The study sections, which variably represent the late Wuchiapingian and Changhsingian stages of the Late Permian and the early Induan Stage of the Early Triassic, have well-established conodont biostratigraphies (e.g., Jiang et al., 2007; Sun et al., 2012; Zhang et al., 2014) (Fig. S1), providing a high-resolution correlation framework within which to study ocean-redox and -chemical variation. The conodont biostratigraphic scheme developed for South China can be summarized as follows (e.g., Jiang et al., 2007; Algeo et al., 2013; Yin et al., 2014): i) the Wuchiapingian-Changhsingian boundary is defined by the first appearance datum (FAD) of *Clarkina wangi (C. wangi)*; ii) the Changhsingian Stage comprises six biozones, including (from oldest to youngest) the *C. wangi*, *C. subcarinata*, *C. changxingensis*, *C. yini*, *C. meishanensis* and *C. zhejiangensis* zones; iii) the Permian-Triassic (or Changhsingian-Induan stage) boundary is defined by the FAD of *Hindeodus parvus (H. parvus)*; iv) in the lower Induan stage, the hindeodid genera *Hindeodus* and *Isarcicella* temporarily dominate over the gondolellid genus *Clarkina* at many localities; and v) the *H. praeparvus-H. latidentatus* zones are biostratigraphically equivalent to the *C. meishanensis* and lower *C. zhejiangensis* zones. Typically, the latest Permian mass extinction (LPME) horizon is defined by a sudden reduction in fossil abundance and a sharp diminution of taxonomic diversity (Fig. S1).

3. Proxy data compilation

3.1. Fe speciation data

Iron (Fe) speciation is commonly used to identify redox facies, with the ratio of highly reactive Fe-to-total Fe (Fe_{HR}/Fe_T) distinguishing oxic (<0.22) from anoxic facies (>0.38, with intermediate values being equivocal), and the ratio of sulfide mineral Fe-to-highly reactive Fe (Fe_{Py}/Fe_{HR}) distinguishing anoxic-ferruginous (<0.70–0.80) from anoxic-euxinic facies (>0.70–0.80) (Poulton and Canfield, 2011; Clarkson et al., 2016; Xiang et al., 2022). A prerequisite for application of Fe-speciation to redox analysis of carbonate sediments is a total Fe content (Fe_T) >0.50 wt% (Clarkson et al., 2014). Fe speciation data can potentially be influenced by early diagenesis, which may change Fe_{HR}/Fe_T and Fe_{Py}/Fe_{HR} but not Fe_T/Al (Clarkson et al., 2014; Eroglu et al., 2021). An average Fe_T/Al ratio of 0.55 ± 0.11 has been proposed for oxic marine facies, with higher ratios for more reducing facies (Clarkson et al., 2014, 2016). Integrated utilization of the Fe_T/Al, Fe_{HR}/Fe_T and Fe_{Py}/Fe_{HR} proxies is adopted in this study in order to reliably identify water-column redox conditions (Fig. 2).

In a middle-shelf setting (Meishan), original Fe speciation data are all from the data supplement of Xiang et al. (2020), and Xiang et al. (2020) didn't illustrate Fe_T/Al ratios. Fe_T/Al ratios vary from 0.15 to 2.25, with an overall increase upwards in the uppermost Permian (*C. changxingensis* to *C. meishanensis* zones), reaching a peak (1.82) at the LPME horizon (Fig. 2) (Xiang et al., 2020). Fe_{HR}/Fe_T (0.31 to 0.88) and Fe_{Py}/Fe_{HR} (0.19 to 0.91) ratios also reach a peak at this level (0.83 and 0.91, respectively). Above the LPME horizon, Fe_T/Al ratios decline abruptly and then remain relatively stable around 0.50 in the lowermost Triassic (*H. parvus* to *I. isarcica* zones). Fe_{HR}/Fe_T and Fe_{Py}/Fe_{HR} ratios decline upwards from 0.50 to 1.00 to 0.00–0.50 with fluctuations from uppermost Permian (*C. meishanensis* Zone) to lowermost Triassic (*H. parvus* to *I. isarcica* zones).

In a middle-shelf setting (Ganxi) with water depths deeper than Meishan, the Fe speciation data are all sourced from Lei et al. (2017), while the Fe_T/Al ratios are not shown in the original study. Fe_T/Al ratios range from 0.00 to 1.68 (Fig. 1C) (Lei et al., 2017). In the uppermost Permian, they increase from the *C. wangi* Zone (mostly 0.23–0.78) to the lower *C. changxingensis* Zone (up to 1.68) and then decrease from the upper *C. changxingensis* Zone (mostly 0.30–0.60) to the *C. meishanensis* Zone (0.00–0.40), followed by an increase into the lowermost Triassic (0.35 to 0.72). The Fe_{HR}/Fe_T (0.27 to 1.00) and Fe_{Py}/Fe_{HR} (0.01 to 0.97) profiles display trends similar to that of Fe_T/Al.

In an outer-shelf setting (Shangsi), all Fe speciation data are from Xiang et al. (2016), and the Fe_T/Al ratios don't show in the origin study. Fe_T/Al ratios are from 0.27 to 1.36, increasing from the *C. subcarinata* Zone (0.32 to 0.54) to the lower *C. changxingensis* Zone (0.33 to 1), and then decreasing from the upper *C. changxingensis* Zone (up to 1.36) to the *C. meishanensis* Zone (0.60 to 0.72), with a subsequent increase in the lowermost Triassic (*H. parvus* to *I. isarcica* zones) (up to 1.00) (Xiang et al., 2016). Fe_{HR}/Fe_T (0.29–0.82) and Fe_{Py}/Fe_{HR} (0.02–0.95) decrease from the *C. subcarinata* to *C. meishanensis* zones and then increase in the lowermost Triassic (*H. parvus* to *I. isarcica* zones).

In a basinal setting (Penglaitan), the Fe speciation data are all sourced from Xiang et al. (2022). Fe_T/Al ranges from 0.22 to 2.01, Fe_{HR}/Fe_T from 0.21 to 0.85, and Fe_{Py}/Fe_{HR} from 0.00 to 0.41 (Xiang et al., 2022). Decreasing Fe_T/Al ratios are associated with lower Fe_{HR}/Fe_T and Fe_{Py}/Fe_{HR} values in the *C. yini* and lower *C. meishanensis* zones. Upsection, Fe_T/Al, Fe_{HR}/Fe_T and Fe_{Py}/Fe_{HR} all show increases before a decline at the LPME horizon, followed by another increase in the lowermost Triassic (*H. parvus* Zone).

Table 1
Sedimentological and marine redox-related information of the studies sections from previous work.

Section	Lithology at the P-Tr transition	Environmental setting	Previous work for investigating marine redox conditions	Main reference
Nhi Tao	Dong Dang Formation of upper Permian: fossiliferous limestone with diverse benthic metazoan fossils, replaced by oolitic-pisolitic limestone at the late Permian event horizon, and this is overlain by microbialites; Hong Ngai Formation of lower Triassic: microbialites	Carbonate platform; water depth: ca. 10–30 m	Total S and P, TOC content, Redox-sensitive elements, $\delta^{34}S_{py}$	Algeo et al., 2007 , 2008; Son et al., 2007
Taiping	Heshan Formation (uppermost Permian): mainly medium bedded bioclastic limestone with diverse metazoan fossils Majiaoling Formation of lowermost Triassic: mainly microbialites in the basal part overlain by oolitic limestone/dolostone.	Carbonate platform; water depth: ca. 10 to 30 m	Framboidal pyrites, $\delta^{34}S_{pyrite}$, $\delta^{15}N$	Luo et al., 2011; Xiao et al., 2018; Tian et al., 2019
Meishan	Changxing Formation of uppermost Permian: mainly thin-bedded bioclastic limestone with diverse benthic metazoan biota; Yinkeng Formation of lowermost Triassic: mainly thin interbedded marlstone and mudstone. A few volcanic ash layers occur in the boundary interval.	Upper carbonate ramp; water depth, 100 to 200 m	Biomarkers, framboidal pyrites, biota diversity, trace fossils, iron speciation, sulfur ($\delta^{34}S_{py}$ and $\delta^{34}S_{CAS}$) analysis, $\delta^{15}N$	Grice et al., 2005; Summons et al., 2006; Luo et al., 2011; Li et al., 2016; Xiang et al., 2020; Song et al., 2013a
Changtanhe	Dalong Formation of uppermost Permian: mainly laminated wackestone, with thin mudstone and shale beds becoming more common toward the top; abundant and diverse benthic metazoan fossils. Daye Formation of lowermost Triassic: mainly lime mudstone, marlstone and micrite limestone.	Upper carbonate ramp	Framboidal pyrites, fossil diversity and TOC content	He et al., 2013
Ganxi	Dalong Formation of uppermost Permian: mainly lime mudstone in the lower part and marly limestone with interbedded lime mudstone in the upper part. Diverse benthic metazoan biota. Daye Formation of lowermost Triassic: mainly lime mudstone. A few volcanic ash beds occur within the uppermost Dalong Formation and the lowermost Daye Formation.	Upper carbonate ramp; water depth: ca. 200 to 300 m	Iron speciation, Mo element, $\delta^{15}N$	Lei et al., 2017; Wu et al., 2022
Jianshi	Dalong Formation of upper Permian: mainly black limestones and mudstones intercalated with gray limestones; Daye Formation of lower Triassic: mainly gray carbonate and calcareous mudstones	Upper carbonate ramp	TOC, $\delta^{15}N$	Wu et al., 2022
Shangsi	Dalong Formation of uppermost Permian (Changhsingian): mainly micrite limestone that is organic-rich in the lower part and chert-rich in the upper part containing radiolarian; Feixianguan Formation of lowermost Triassic (Induan): mainly thin-bedded alternations of micrite and argillaceous limestones.	Lower carbonate ramp and deeper; water depth: 100–300 m	Iron speciation, redox-sensitive elements, fossil diversity, bioturbation degree, sulfur ($\delta^{34}S_{py}$ and $\delta^{34}S_{CAS}$) analysis, TOC, P	Wignall et al., 1995; Bond and Wignall, 2010; Xiang et al., 2016; Xiao et al., 2017
Chibi	Dalong Formation (upper Permian): mainly dark gray to black siliceous carbonates and cherts with sponge spicules and radiolarian test; Daye Formation (lower Triassic): thinly bedded, in part dolomitic light gray carbonates and marls	Lower carbonate ramp and deeper	TOC content, P speciation, TOC/P, framboidal pyrite, biodiversity, redox-sensitive elements,	Li et al., 2022; Müller et al., 2022
Chaotian	upper Dalong Formation of uppermost Permian (late Changhsingian): frequently bioturbated and consists mainly of calcareous/cherty (lime)mudstone with micritic limestone at the top; abundant ammonoids, conodonts and radiolarians. Feixianguan Formation of lower Triassic: largely unbioturbated and consists of micrite limestone with a basal marl bed that is barren of fossils but contains abundant pyrites	Lower carbonate ramp and deeper	Framboidal pyrites, bioturbation, trace fossils, TOC content, $\delta^{34}S_{py}$, $\delta^{15}N$	Newton et al., 2009; Saitoh et al., 2021; Wu et al., 2022
Xiaojiaba	upper Permian Dalong Formation: mainly lime mud-rich chert in its lower and middle parts, and lime mudstone and siliceous or nodular limestone in its upper part. Volcanic tuff layers are abundant in the upper part, but only a few occur in the lower and middle parts. Abundant brachiopods, gastropods, ammonoids and radiolarian Feixianguan Formation of lower Triassic: mainly interbedded shale and lime mudstone. Many volcanic tuff layers are present near the base of the Feixianguan Formation, and no fossils are recorded in its lower part.	Lower carbonate ramp and deeper	Framboidal pyrite, $\delta^{34}S_{py}$, C_{org}/P, Mo_{auth} and U_{auth},	Wei et al., 2015
Penglaitan	Talung Formation of uppermost Permian: mainly mixed carbonate-siliciclastic-tuffaceous-chert sediments. Abundant radiolarian and ammonoids Luolou Formation of lowermost Triassic: mainly interbedded lime mudstone and micrite limestone.	Basin	Iron speciation and redox-sensitive elements, biodiversity	Shen et al., 2019; Xiang et al., 2022

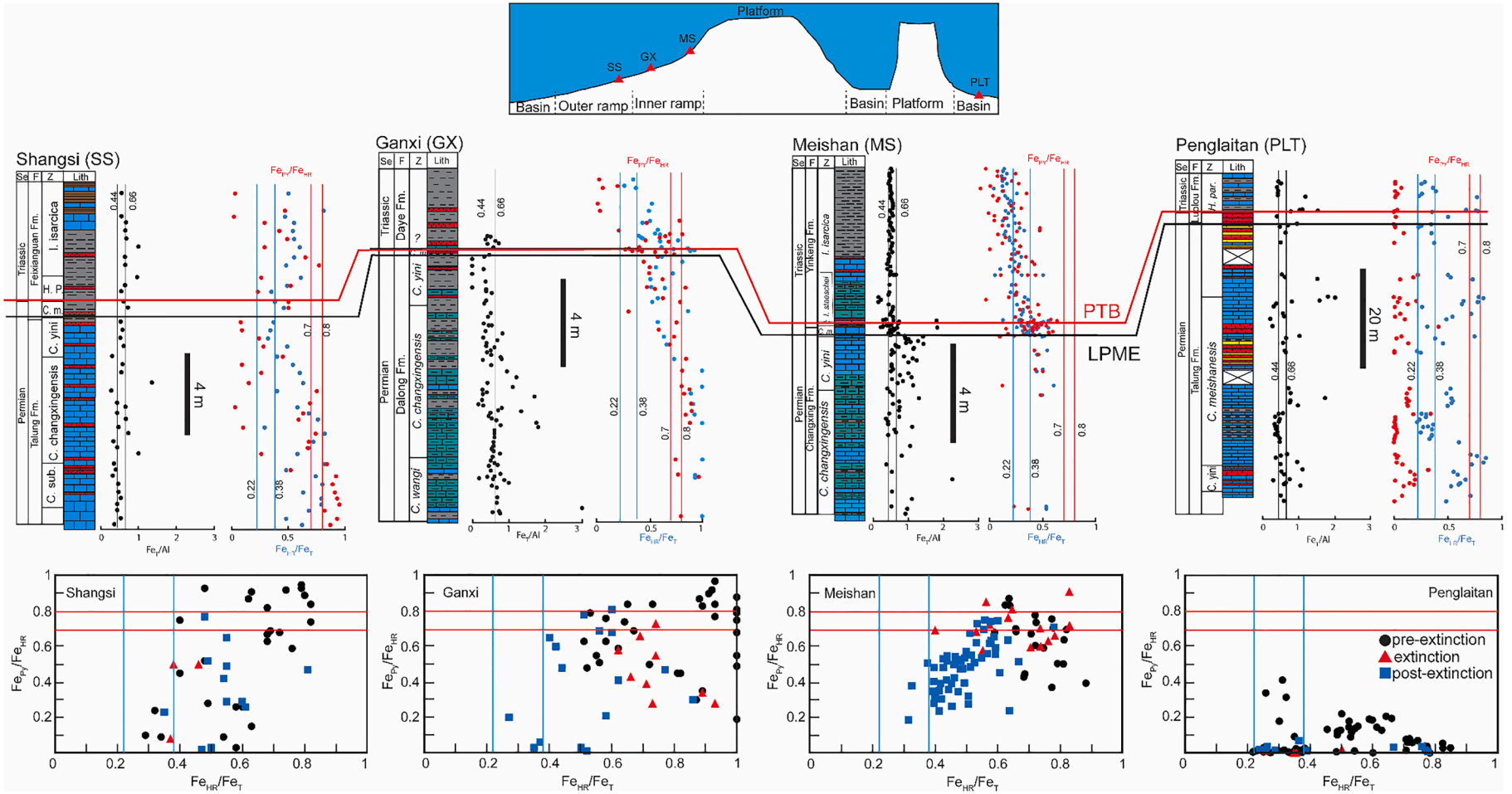

Fig. 2. Proximal-to-distal Fe-speciation data. Data sources: Meishan, Xiang et al. (2020); Ganxi, Lei et al. (2017); Shangsi, Xiang et al. (2016); Penglaitan, Xiang et al. (2022). Abbreviations: LPME–latest Permian mass extinction, PTB–Permian-Triassic boundary. See Fig. 3 for lithologic legend.

3.2. Pyrite framboid size distributions

The size distribution of pyrite framboids is also commonly used to evaluate marine redox conditions (Bond and Wignall, 2010; He et al., 2013; Li et al., 2016). In euxinic water columns, pyrite framboids tend to form rapidly and abundantly but reach a small maximum size before settling to the sediment-water interface. By contrast, in dysoxic porewaters, pyrite framboids have more time to grow and therefore achieve larger sizes, although a smaller number of framboids are generally nucleated (Wilkin et al., 1996; Wilkin and Barnes, 1997; Wignall and Newton, 1998).

In inner-shelf (Taiping) and middle-shelf (Meishan) settings, the pyrite framboid data are from Li et al. (2016) and Xiao et al. (2018). The mean diameters of pyrite framboids range between 4 and 9 μm. They decrease from the pre-LPME Upper Permian (mean ~ 6 to 7 μm) to the LPME horizon (mean ~ 4 to 5 μm). In the overlying *H. parvus* to *I. staeschi-I. isarcica* zones (Fig. 3), pyrite framboids are characterized by: i) an increase of mean size to 15 μm in the lower *H. parvus* Zone, followed by a decrease of mean size to 7 to 9 μm in the upper *H. parvus* Zone in the shallower Taiping section; ii) an increase of mean size, reaching to 8 μm, in the *H. parvus* Zone, and an absence of pyrite framboids in the lower *I. staeschi-I. isarcica* zones before the recurrence of pyrite framboids (mean size ~5 μm) in the deeper Meishan section (Fig. 3).

In a middle shelf setting (Changtahe) with water depths deeper than that of Taiping and Meishan, pyrite framboids (data sourced from He et al., 2013) range in mean diameter between 5 and 12 μm. They decrease from the pre-LPME Upper Permian (mean 7–9 μm) to the LPME horizon (mean 5–6 μm). Mean pyrite framboid size increases to 10.5 μm just above the LPME, and then decreases to 6–7 μm in the lowermost Triassic.

In outer-shelf settings (Chaotian and Xiaojiaba), pyrite framboids (data from: Wei et al., 2015; Saitoh et al., 2021) range in mean diameter between 3 and 23 μm. They occur rarely or increase in size (up to 30 μm) at the LPME horizon. Between the LPME horizon and the P-Tr boundary, pyrite framboids are rare in the Chaotian section, but increase in mean size (up to 23 μm) in the Xiaojiaba section. Upwards, in the *H. parvus* Zone, mean sizes of pyrite framboids decrease upwards from 5 to 3 μm in the Chaotian section, and decrease from 23 to 6 μm in the Xiaojiaba section.

3.3. Sulfur-isotope compositions

The sulfur (S) isotopic compositions of both carbonate-associated sulfate ($\delta^{34}S_{CAS}$) and pyrite sulfur ($\delta^{34}S_{py}$) are useful proxies to investigate the marine sulfur cycle. In marine carbonates, $\delta^{34}S_{CAS}$ generally records the ambient isotopic composition of seawater sulfate, and variation in this proxy may reflect influences by riverine flux, evaporation, ocean mixing and marine-redox conditions (e.g., Newton et al., 2004; Kaiho et al., 2006; Riccardi et al., 2006; Luo et al., 2010). Pyrite S-isotopic compositions are often used to evaluate marine redox conditions, as enhanced pyrite burial can cause a shift toward heavier $\delta^{34}S_{py}$. However, terrestrial sulfur inputs and/or upwelling of deep-ocean sulfide may also locally influence sediment $\delta^{34}S_{py}$ via affecting sulfate concentration and/or sulfur isotope of fluids where pyrites may form (e.g., Newton et al., 2004; Algeo et al., 2007; Xiao et al., 2018; Saitoh et al., 2021). Generally, both microbial sulfate reduction (MSR) and pyrite burial lead to higher $\delta^{34}S_{py}$ and $\delta^{34}S_{CAS}$ values, whereas marine pyrite oxidation and the influx of isotopically light riverine sulfur (^{32}S) cause lower $\delta^{34}S_{py}$ and $\delta^{34}S_{CAS}$ values (Newton et al., 2004; Riccardi et al., 2006; Algeo et al., 2007; Luo et al., 2010).

In inner-shelf and shallow middle-shelf settings with $\delta^{34}S$ ($\delta^{34}S_{py}$ and $\delta^{34}S_{CAS}$) from Kaiho et al. (2006), Riccardi et al. (2006), Algeo et al. (2007, 2008) and Xiao et al. (2018). $\delta^{34}S_{py}$ ranges from ca. –30‰ to +10‰ at Taiping, from −38‰ to +14‰ at Nhi Tao, and from −35‰ to +5‰ at Meishan, while $\delta^{34}S_{CAS}$ ranges from ca. 0‰ to +29‰ in Meishan. $\delta^{34}S_{py}$ increases to ca. +5‰ in the lower part of *C. yini-C. meishanensis* zones (as shown in Taiping and Meishan) and then decreases (to ca. –30‰) overall from the upper part of *C. yini-C. meishanensis* zones in the uppermost Permian to the *H. parvus* Zone in the lowermost Triassic (Fig. 4). Similar trends are also observed for $\delta^{34}S_{CAS}$, which increases up to +29‰ immediately below the LPME, and then decreases from the uppermost Permian (*C. yini-C. meishanensis*) to the lowermost Triassic (*H. parvus to I. staeschei*).

In outer-shelf settings (Shangsi and Chaotian) with $\delta^{34}S$ ($\delta^{34}S_{py}$ and $\delta^{34}S_{CAS}$) from Riccardi et al. (2006) and Saitoh et al. (2021), $\delta^{34}S_{py}$ ranges from ca. –50‰ to −10‰, and $\delta^{34}S_{CAS}$ values range from −20‰ to +30‰ (Fig. 4). Both $\delta^{34}S_{py}$ and $\delta^{34}S_{CAS}$ increase from the uppermost Permian to the lowermost Triassic (upper *C. changxingensis* to *I. isarcica*). At Shangsi, 20‰ positive excursions of both $\delta^{34}S_{py}$ and $\delta^{34}S_{CAS}$ are observed in the *C. wangi* to lower *C. changxingensis* zones.

In both middle- and outer-shelf settings, around the LPME horizon, short-term negative excursions characterize both $\delta^{34}S_{py}$ (ca. 10–30‰) and $\delta^{34}S_{CAS}$ (ca. 10–20‰). Notably, the stratigraphic occurrence of the negative $\delta^{34}S_{py}$ and $\delta^{34}S_{CAS}$ excursions is different in middle-shelf and outer-shelf settings: the negative excursions occur below the LPME level in the middle-shelf settings, but between LPME and PTB in the outer-shelf settings.

3.4. TOC/P and P speciation data

The ratio of total organic carbon to total phosphorus (TOC/P_{tot}) is a useful benthic redox proxy in many depositional systems (Algeo and Ingall, 2007; Müller et al., 2022). Higher (lower) values of TOC/P_{tot} are associated with more (less) strongly reducing conditions, which enhance (limit) organic carbon preservation while simultaneously liberating (retaining) phosphorus in the sediment. In modern depositional systems, TOC/P_{tot} values of <50, 50 to 100–125, and > 100–125 were suggested to be associated with oxic, suboxic, and euxinic environments, respectively (Algeo and Ingall, 2007). However, other factors (e.g., primary productivity, ocean mixing, and riverine flux) can also be important to influence TOC/P_{tot} ratios (Algeo et al., 2007; Xiang et al., 2016; Schobben et al., 2020; Müller et al., 2022).

With regard to P-Tr transition sections, an inner-shelf setting (Nhi Tao), where original TOC and P_{tot} data are from Algeo et al. (2007, 2008), shows TOC/P_{tot} increasing from the *C. yini-C. meishanesis* to the *H. parvus-I. isarcica* zones, as suggested by the TOC decrease from >0.5% to <0.1% and coeval P_{tot} increase (from ~0% to >0.04%).

In outer shelf-settings, (Xiaojiaba and Chibi), original TOC/P_{tot} data are from Wei et al. (2015) for the Xiaojiaba section, and from Müller et al. (2022) for the Chibi section. Original TOC and P_{tot} data in the Shangsi section are from Xiang et al. (2016). The TOC/P_{tot} values vary mostly between >106 to 500, with a decrease in the *C. changxingensis* Zone and remaining low (⟨100) in the extinction interval (*C. yini* to *C. meishanesis* zones) and lowermost Triassic (*H. parvus* to *I. isarcica* zones) (Fig. 5).

Along with TOC/P_{tot}, phosphorus speciation analysis can be useful in determining the source and processes influencing P accumulation in the sediment (Schobben et al., 2020; Müller et al., 2022). Total phosphorus (P_{tot}) is the sum of detrital P (P_{det}) plus multiple reactive P (P_{reac}) fractions (where $P_{reac} = P_{tot} - P_{det}$), including loosely adsorbed phosphorus (P_{ex}), authigenic apatite-P (P_{auth}), P bound to organic matter (P_{org}), and Fe-oxyhydroxide-bound P (P_{Fe}) (Ruttenberg et al., 2009). P speciation data were compiled in this study from Müller et al. (2022), where available, although most P-Tr studies have reported only P_{tot} concentrations, sometimes in an Al-normalized form (i.e., P_{tot}/Al) (Fig. 5) (data from Wei et al., 2015; Xiang et al., 2016; Müller et al., 2022).

As for P_{tot}/Al ratios, the original data are from Wei et al. (2015), Xiang et al. (2016) and Müller et al. (2022). The P_{tot}/Al ratios range mainly between 0 and 0.4, and they decrease upward from the uppermost Permian to the lowermost Triassic in the outer-shelf settings. Despite fluctuations, overall higher P_{tot}/Al ratios (often >0.1) are found at Shangsi than in the deeper Chibi and Xiaojiaba sections (typically

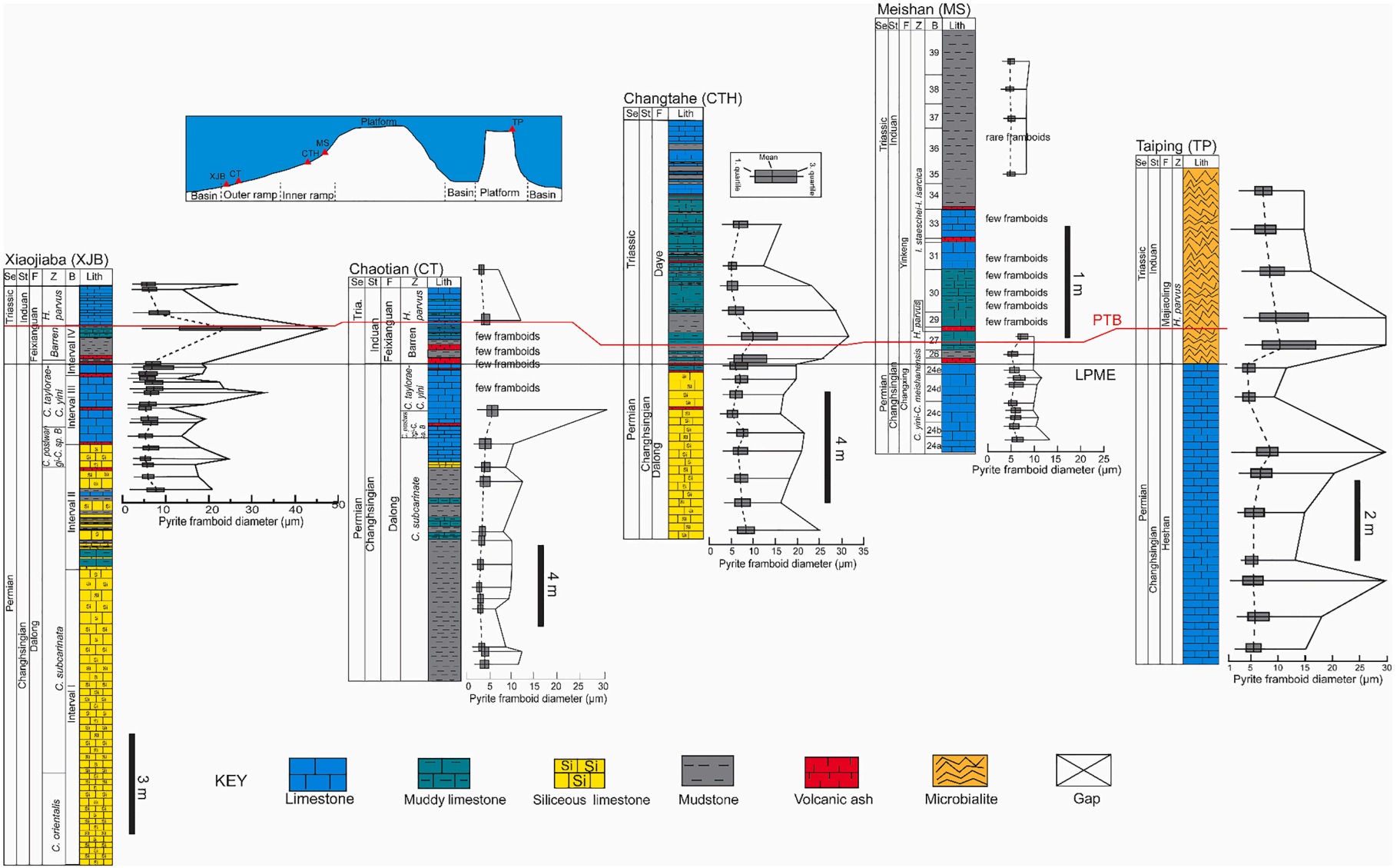

Fig. 3. Proximal-to-distal pyrite distribution data. Data sources: Taiping, Xiao et al. (2018); Meishan, Li et al. (2016); Changtahe, He et al. (2013); Chaotian, Saitoh et al. (2021); Xiaojiaba, Wei et al. (2015). See Fig. 2 for other details.

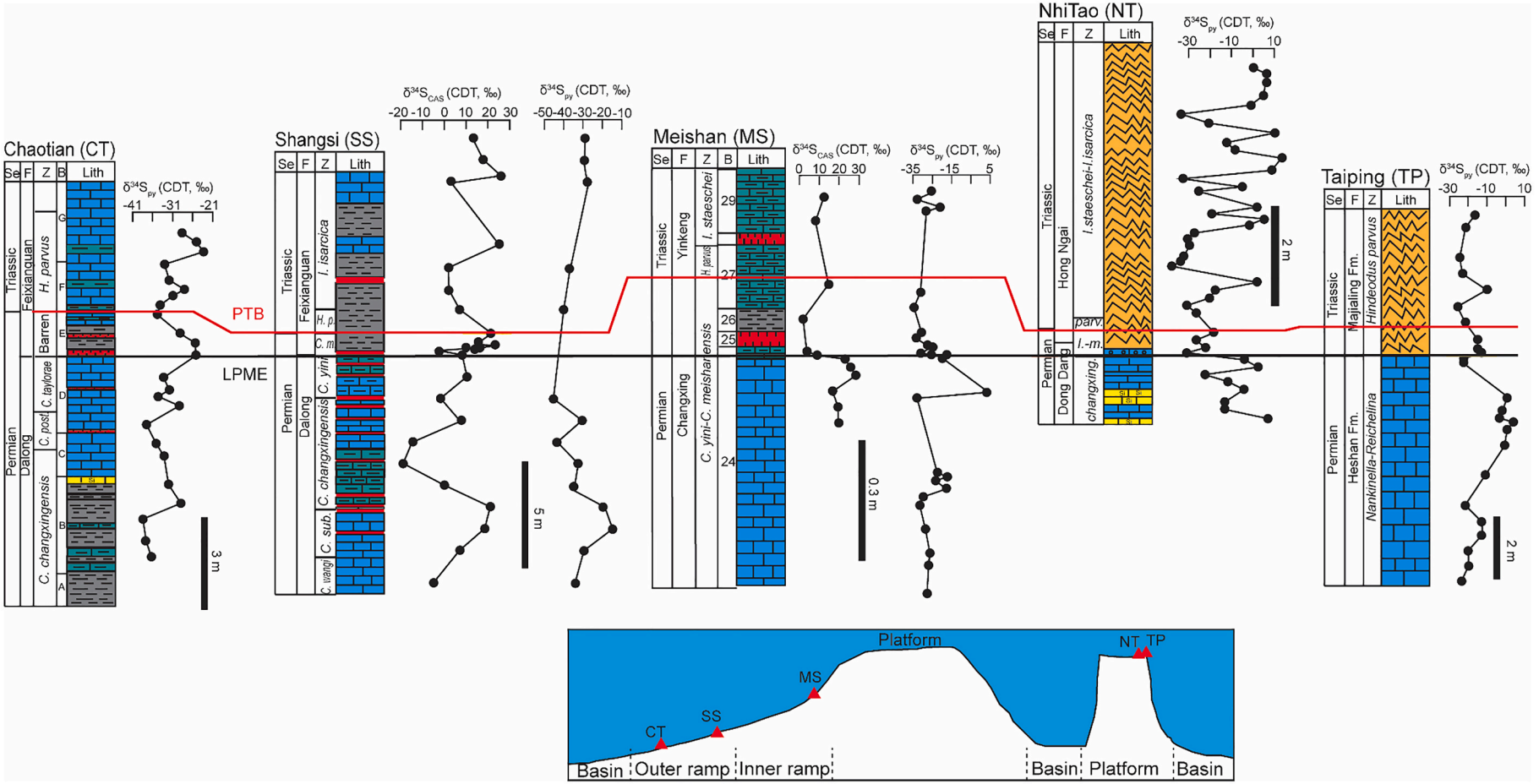

Fig. 4. Proximal-to-distal distribution of $\delta^{34}S$ ($\delta^{34}S_{py}$ and $\delta^{34}S_{CAS}$) data. Data sources: Taiping, Xiao et al. (2018); Nhi Tao, Algeo et al. (2007, 2008); Meishan, Kaiho et al. (2006), Riccardi et al. (2006); Shangsi, Riccardi et al. (2006); Chaotian, Saitoh et al. (2021). See Fig. 3 for lithologic legend and Fig. 2 for other details.

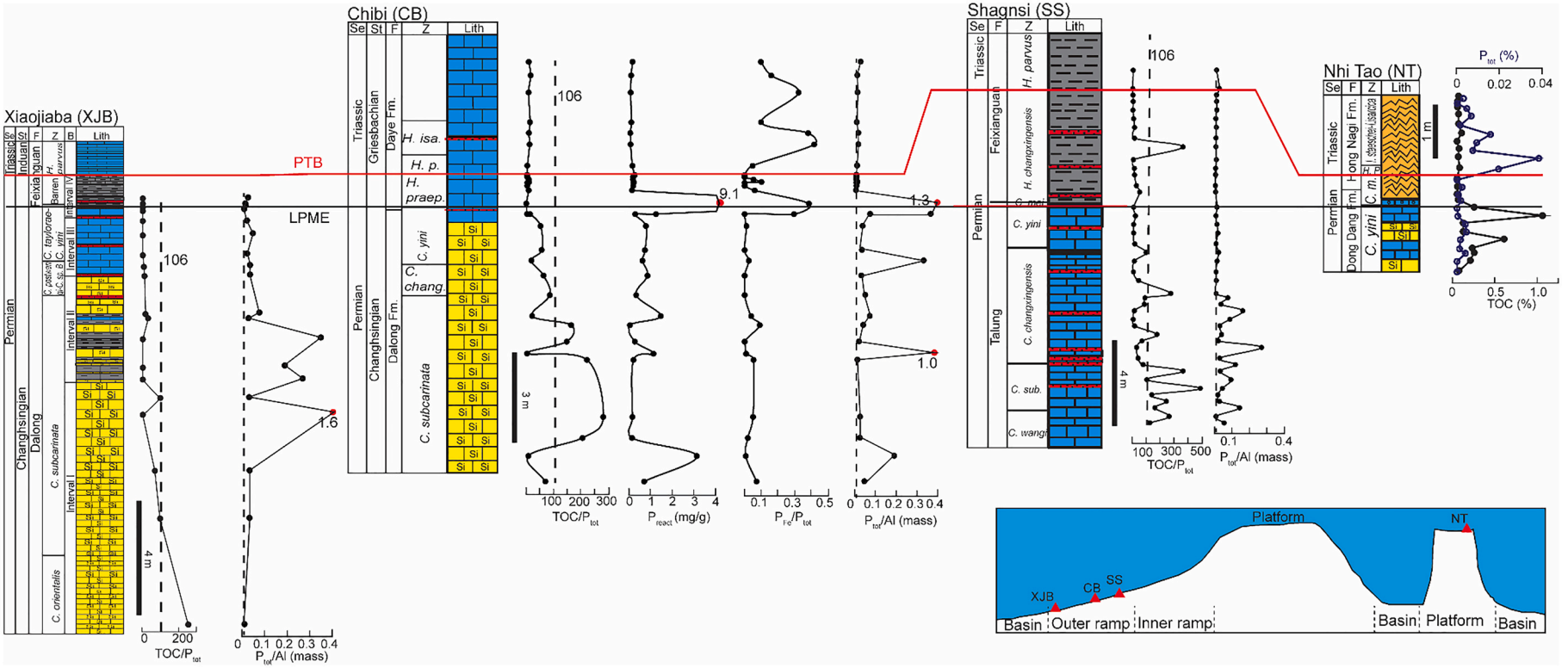

Fig. 5. Proximal-to-distal distribution of P data. Data sources: Nhi Tao, Algeo et al. (2007, 2008); Shangsi, Xiang et al. (2016); Chibi, Müller et al. (2022); Xiaojiaba, Wei et al. (2015). Abbreviations: TOC–total organic carbon; P_{tot}–total P; P_{reac}–bioavailable P; P_{Fe}–Fe-oxyhydroxide-bound P. For the TOC/P_{tot}, the vertical dashed line indicates a value of 106 (Redfield ratio). For the P_{tot}/Al, the vertical dashed line indicates a value of 0.008 (average shale reference value). The red dots indicate outliers. See Fig. 3 for lithologic legend and Fig. 2 for other details. (For interpretation of the references to colour in this figure legend, the reader is referred to the web version of this article.)

<0.1) where some outliers exist. At Chibi (P speciation data from Müller et al., 2022), P_{Fe}/P_{tot} ratios (0.00 to 0.42) are higher in the lowermost Triassic (up to 0.42) relative to the uppermost Permian (0.00 to 0.09), while P_{reac} (0 to 9.1 mg/g) values decrease upwards from the uppermost Permian to the lowermost Triassic.

3.5. $\delta^{15}N_{org}$ compositions

Nitrogen is highly relevant in terms of marine productivity, marine organic carbon fluxes and climatic evolution (Robinson et al., 2012). N fixation by cyanobacteria is the most important source of marine bioavailable N (Sigman and Casciotti, 2001; Robinson et al., 2012; Algeo et al., 2014). The bioavailable N is mainly consumed by assimilatory uptake and denitrification processes (Robinson et al., 2012; Algeo et al., 2014; Wu et al., 2022). Generally, due to quantitative utilization of fixed N, the N-isotope fractionation during assimilatory uptake is limited (Sigman and Casciotti, 2001; Robinson et al., 2012). Consequently, marine $\delta^{15}N_{org}$ variation can provide valuable information about nitrogen fixation and denitrification processes (Gruber, 2008). Typically, nitrogen fixation leads to lower $\delta^{15}N_{org}$ by transferring isotopically light N from the atmosphere, while denitrification causes higher $\delta^{15}N_{org}$ by releasing isotopically light N back to the atmosphere (Luo et al., 2011; Wu et al., 2022). Notably, nitrate-rich settings also yield lower $\delta^{15}N_{org}$ owing to a negative fractionation during bioassimilation that does not find expression in nitrate-poor settings in which nitrate utilization is quantitative (Calvert et al., 1992).

The $\delta^{15}N_{org}$ data herein are collected from Luo et al. (2011) and Wu et al. (2022) (Fig. 6). In the uppermost Permian, $\delta^{15}N_{org}$ ranges between +2‰ and + 4‰ in the inner-and middle-shelf settings (Taiping, Meishan, Ganxi and Jiangshi), but are between 0‰ and + 2‰ in outer-shelf settings (Chaotian) (Fig. 6). Notably, lower $^{15}N_{org}$ occurs with increasing water depth from inner- to outer-shelf settings. In the inner- (Taiping) and middle-shelf settings (Meishan, Ganxi and Jiangshi) (Luo et al., 2011; Wu et al., 2022), $\delta^{15}N_{org}$ abruptly decreased by 3–4‰ between the LPME and the PTB. In outer-shelf settings (Chaotian) (Wu et al., 2022), $\delta^{15}N_{org}$ decreases upwards in the uppermost Permian, but the decreasing trend is characterized by: i) a smaller decreasing magnitude (1–2‰); and ii) earlier occurrence (below the LPME) than that in the inner- and middle shelf settings. In the lowermost Triassic, $\delta^{15}N_{org}$ is unified to be ca. 0‰ in both inner-, middle- and outer-shelf settings. The $\delta^{15}N_{org}$ decreases to around 0‰ earlier in deepwater settings (i.e., in the *C. changxingensis* Zone or earlier) than in shallow-water settings (in the *C. meishanensis* Zone).

4. Discussion

Decoding the extent and intensity of oceanic de-oxygenation and its relationship to the marine sulfur and nutrient cycles is important to evaluating environmental scenarios for the LPME crisis in South China. In the following, we will examine oceanographic variation across the South China Craton during the P-Tr transition with regard to redox conditions (Section 4.1), their relationship to seawater sulfate (Section 4.2) and nutrient status (Section 4.3), and general implications for the LPME (Section 4.4).

4.1. Extent and intensity of marine de-oxygenation

Based on Fe speciation data, the *C. wangi/C. subcarinata* to lower *C. changxingensis* zones are characterized by Fe_{HR}/Fe_T and Fe_{Py}/Fe_{HR} ratios consistent with euxinic conditions in deeper middle-shelf and outer-shelf settings, as recorded previously at Ganxi by Lei et al. (2017) and Shangsi by Xiang et al. (2016) (Fig. 2). In a shallower middle-shelf setting (Meishan), where Fe_T is <0.5 wt%, the occurrences of abundant macro- and trace fossils and complex burrow systems, as well as multiple S isotope (^{32}S, ^{33}S, ^{34}S and ^{36}S) analysis of pyrite were suggested to reflect mainly oxic conditions in previous studies (Shen et al., 2011; Xiang et al., 2020).

In the overlying upper *C. changxingensis* to *C. yini-C. meishanensis* zones, decreases in Fe_T/Al, Fe_{HR}/Fe_T and Fe_{Py}/Fe_{HR} (Fig. 2) reflect a change to mainly anoxic and ferruginous conditions in deeper middle-shelf (Ganxi) to basinal settings (Penglaitan), as have been proposed by Lei et al. (2017) and Xiang et al. (2022). A brief oxygenation event may have happened during the LPME in deeper middle-shelf to basinal settings, as evidenced by a decreased abundance and increased size of pyrite framboids (Fig. 3). Moreover, increases in Fe/Al, Fe_{HR}/Fe_T and Fe_{Py}/Fe_{HR} are suggestive of strong de-oxygenation and development of euxinic conditions in the shallower water depth of middle-shelf settings (Meishan) (Fig. 2), which is supported by the greater abundance and smaller size of pyrite framboids (Fig. 3).

The lowermost Triassic (*H. parvus* to *I. isarcica* zones) is characterized by increases in Fe_T/Al and Fe_{HR}/Fe_T but a decrease in Fe_{Py}/Fe_{HR} (Fig. 2), indicative of anoxic ferruginous conditions in deeper middle-shelf to basinal settings. This is consistent with pyrite framboids with a large size range (Fig. 3). In shallower middle-shelf settings, decreases in Fe_T/Al, Fe_{HR}/Fe_T and Fe_{Py}/Fe_{HR} (Fig. 2) are indicative of increased oxygenation and a shift to variably oxic to ferruginous conditions, supported by the occurrence of few pyrite framboids (Fig. 3).

To summarize, in a temporal and spatial context, from latest Permian to earliest Triassic, basinal settings may remain mainly ferruginous conditions, deeper middle-shelf to outer-shelf settings changed in dominance from euxinic to ferruginous conditions, while shallower middle-shelf settings evolved from oxic to euxinic to ferruginous-anoxic conditions (Fig. 7). Moreover, the LPME horizon was characterized by a transient oxygenation event in deeper middle-shelf to basinal settings (He et al., 2013; Wei et al., 2015) co-occurring with an enhanced oxygenation depletion in shallower middle-shelf settings (Li et al., 2016). This transient deep-water oxygenation event has been also reported from elsewhere in the Paleotethys (Newton et al., 2004) and Panthalassa oceans (Newby et al., 2021).

4.2. Relationship between marine de-oxygenation and seawater sulfate

As discussed above, the extent and magnitude of marine de-oxygenation varied spatially and temporarily during the P-Tr transition. The redox evolution has a close relation with seawater sulfur cycles (Newton et al., 2004; Riccardi et al., 2006; Xiao et al., 2018; Saitoh et al., 2021). In the uppermost Permian (*C. yini-C. meishanensis* zones), a secular decrease in $\delta^{34}S$ values (both $\delta^{34}S_{py}$ and $\delta^{34}S_{CAS}$) in shallower middle-shelf settings (e.g., Meishan) (Fig. 4) coincided with de-oxygenation and the development of euxinic conditions. These scenarios require a sufficient supply of SO_4, and sources of isotopically light S (^{32}S) and organic matter (Kaiho et al., 2006; Algeo et al., 2007; Shen et al., 2011). Moreover, in outer-shelf settings, secular increases in $\delta^{34}S$ (both $\delta^{34}S_{py}$ and $\delta^{34}S_{CAS}$) (Fig. 4) were accompanied by mainly anoxic and ferruginous conditions, which may indicate a deficiency of seawater SO_4 content and/or enhanced burial of isotopically light S (^{32}S) (Newton et al., 2004; Riccardi et al., 2006; Luo et al., 2010). Possibly, the incursion of accumulated H_2S (enriched in ^{32}S by MSR) from deep-ocean euxinic waters via chemocline-upward excursions (Kump et al., 2005) or upwelling (Algeo et al., 2007, 2008) can produce lower $\delta^{34}S$ (both $\delta^{34}S_{py}$ and $\delta^{34}S_{CAS}$) values in the ocean-surface layer, but this scenario requires deepwater euxinia. Although ferruginous conditions in deep-marine (outer shelf to basinal) settings were documented in the *C. yini-C. meishanensis* zones in the South China area (Fig. 2), deep-ocean euxinia may have existed elsewhere (e.g., Wignall and Twitchett, 1996; Grice et al., 2005).

Additionally, possible continental influx of light S (^{32}S) might have some influences on the marine $\delta^{34}S$ records. In the *C. yini-C. meishanensis* zones, increased continental light S (^{32}S) influx might originate from volcanic S inputs (Kaiho et al., 2006; Algeo et al., 2007; Yin et al., 2014). Furthermore, terrestrial P-Tr sections reported enhanced accumulation of sulfide with a negative $\delta^{34}S_{py}$ excursion and a fungal event around the

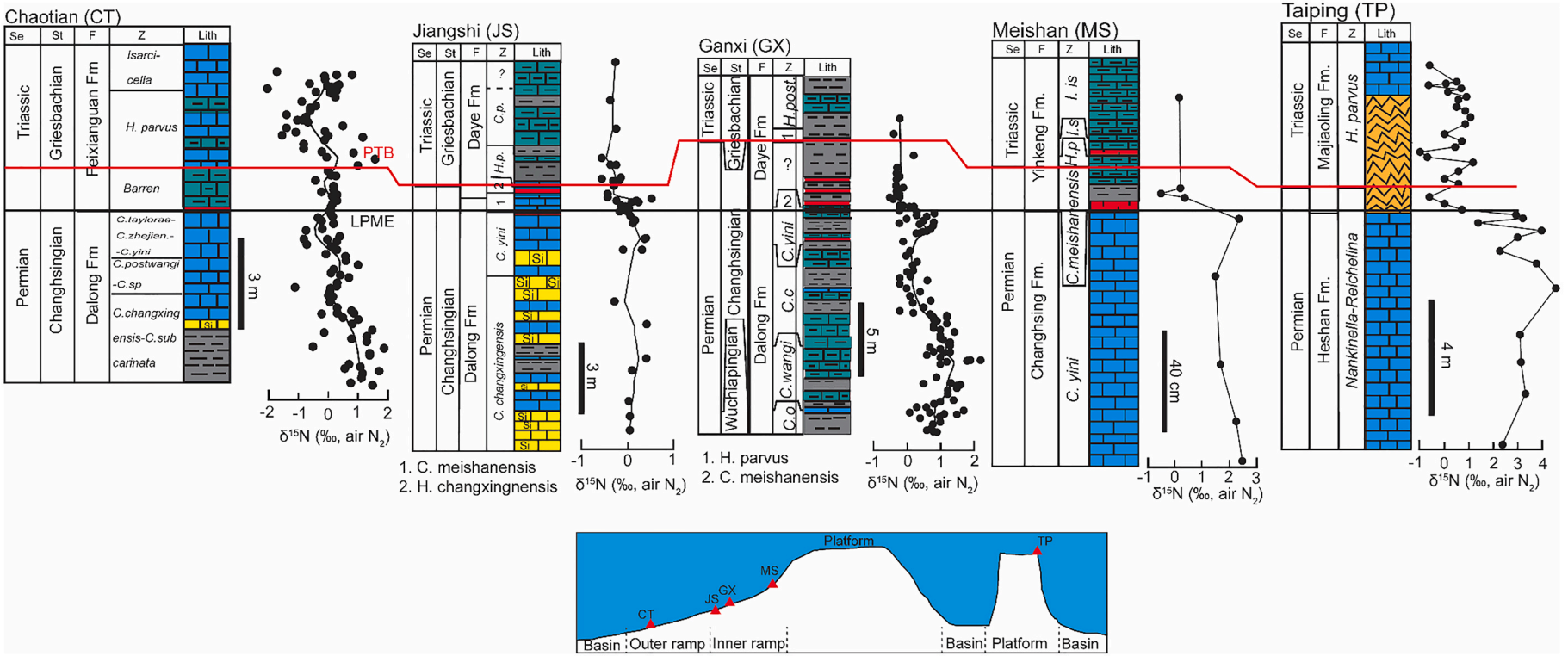

Fig. 6. Proximal to distal distribution of $\delta^{15}N_{org}$ data. Data sources: Luo et al. (2011), Wu et al. (2022). See Fig. 3 for lithologic legend and Fig. 2 for other details.

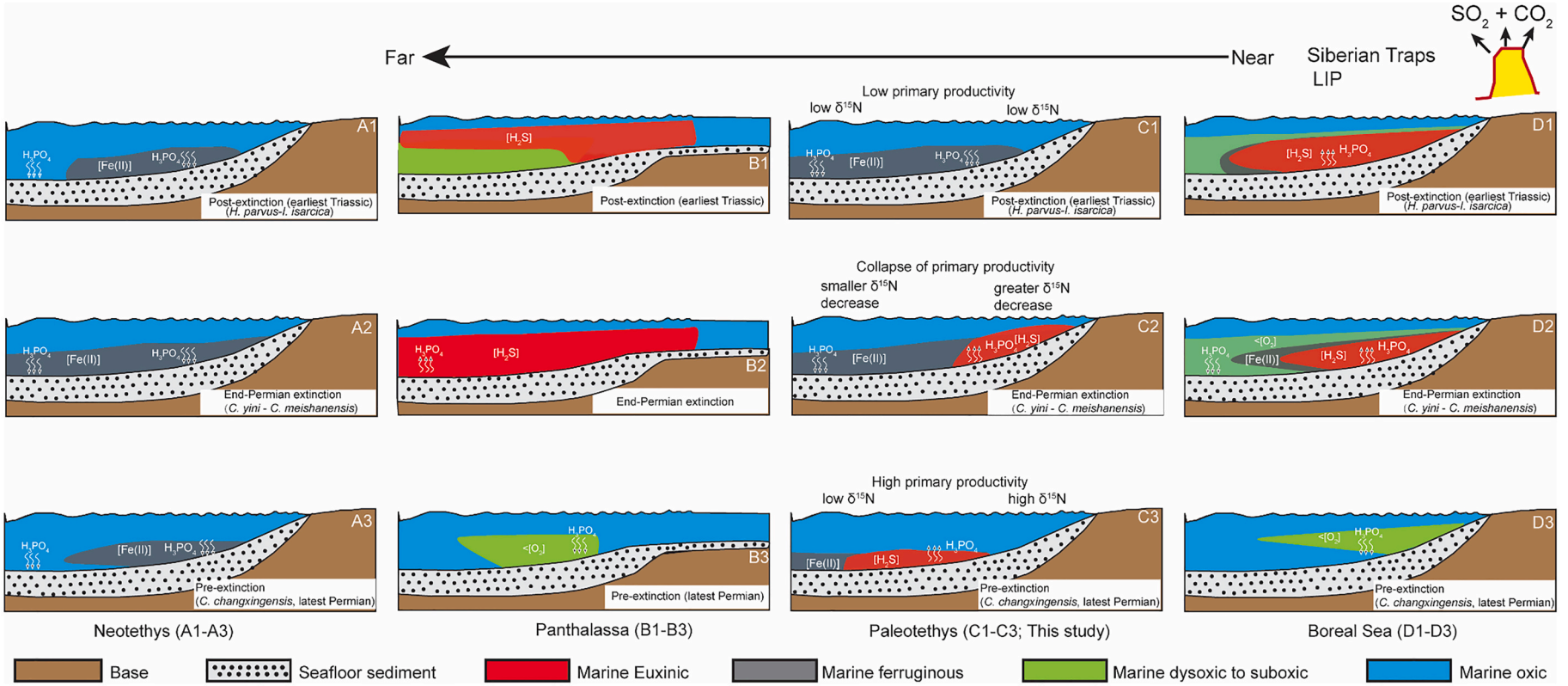

Fig. 7. Conceptual models of spatial and temporal variation in marine redox conditions in the Neotethys, Panthalassa, Paleotethys and Boreal Sea. Neotethys model modified from Clarkson et al. (2016), Panthalassa model modified from Algeo et al. (2010, 2011), and Boreal Sea model modified from Schobben et al. (2020). Notes: Euxinic conditions are indicated by [H_2S]; ferruginous conditions by [Fe(II)]; and dysoxic to suboxic conditions by <[O_2]. With proximity to the Siberian Traps Large Igneous Province, the extent and intensity of marine de-oxygenation are overall enhanced.

P-Tr boundary, and this was attributed to acid rain linked to STLIP sulfate emissions (Maruoka et al., 2003; Brookfield et al., 2018). The enhanced flux of this volcanically-sourced or -related, isotopically light S may have promoted MSR, de-oxygenation, and expansion of euxinia in shallow inner-shelf settings (Kaiho et al., 2006). These processes are supported by evidence of coeval volcanic activity and continental deforestation, which may have promoted an enhanced flux of sulfur and organic material to shallow-marine settings (Kaiho et al., 2006; Xie et al., 2007). Development of anoxic ferruginous conditions in deep-shelf to basinal settings could be explained by a reduced influence of continental sulfur fluxes with increasing distance from land.

4.3. Relationship between marine de-oxygenation and nutrient (N, P) status

Changes in marine redox conditions during the P-Tr transitions also had significant implications for nutrient (N, P) cycles. The recycling of remineralized nutrient elements (N, P) is vital for shallow-marine primary productivity (Robinson et al., 2012; Schobben et al., 2020; Müller et al., 2022). As discussed above, deeper middle-shelf to outer-shelf settings changed from euxinic-ferruginous to mainly ferruginous conditions from the latest Permian to early Triassic, which possibly reduced the in situ recycling of P that actively occurs in euxinic environments (Algeo and Ingall, 2007) and increased P burial (Wei et al., 2015; Müller et al., 2022). In outer-shelf settings, upward-decreasing ratios of total organic carbon to total P (TOC/P_{tot}) (Fig. 5) conformed to enhanced P burial in a shift from euxinic-ferruginous to mainly ferruginous conditions.

The P_{tot}/Al values also decreased rather than increased from the uppermost Permian to the lowermost Triassic in outer-shelf settings, which is inconsistent with enhanced P burial (Fig. 5). Alternatively, in combination with decreasing P_{reac} and increasing P_{Fe}/P_{tot}, this suggests reduced organic production and deposition, while the P is mainly trapped by Fe-oxide, consistent with ferruginous conditions (Müller et al., 2022). On the other hand, the increased TOC/P_{tot} ratios immediately below the LPME horizon in shallower inner-shelf settings (Nhi Tao) (Fig. 5) is consistent with the occurrence of euxinic conditions.

For the $\delta^{15}N_{org}$ signal, as mentioned above, in a whole view, its negative or positive shift mainly depends on the relative importance of nitrogen fixation (leading to lower $\delta^{15}N_{org}$) to denitrification (leading to higher $\delta^{15}N_{org}$) (Sigman and Casciotti, 2001; Robinson et al., 2012). In the uppermost Permian, higher $\delta^{15}N_{org}$ values in middle-shelf settings indicate the process of denitrification associated with high primary productivity (Sigman and Casciotti, 2001; Shen et al., 2015; Wu et al., 2022). From the uppermost Permian to lowest Triassic, the $\delta^{15}N_{org}$ decrease may attribute to: i) enhanced nitrogen fixation; ii) reduced denitrification in the water column. In previous studies, enhanced nitrogen fixation has been typically proposed to account for the $\delta^{15}N_{org}$ decrease (Luo et al., 2011; Sun et al., 2019; Wu et al., 2022) (Fig. 6).

In the South China area, the magnitude of the $\delta^{15}N_{org}$ decrease is positively correlated with the degree of marine de-oxygenation, with a larger $\delta^{15}N_{org}$ decrease in shallow-marine settings in which marine euxinia was intense (Figs. 2 and 6). Possibly, enhanced seawater deoxygenation during the P-Tr transition favored decreases in $\delta^{15}N_{org}$ by promoting i) nitrogen fixation, ii) limiting nitrification and subsequent denitrification, and/or iii) the development of ammonium ocean (Boyle et al., 2013; Sun et al., 2019). However, to what degree the nitrogen fixation was enhanced is not clear. Notably, nutrient elements (Fe, Mo) are needed to facilitate the nitrogen fixation, but a Mo depletion was reported during the P-Tr transition in the Tethys and Panthalassa (Takahashi et al., 2014; Sun et al., 2019). As suggested by Sun et al. (2019), associated with the $\delta^{15}N_{org}$ decrease, there may experience a change of nitrogen fixation from Mo to V—Fe nitrogenase in shallower, N-poor ocean and a development of deeper ammonium ocean.

In the lowermost Triassic, oxic inner-shelf waters became favorable for nitrate formation rather than nitrogen fixation. Although biomarkers indicating the presence of diazotrophic cyanobacteria for nitrogen fixation have been found in the deepwater facies, they were very scarce in shallow water settings (Luo et al., 2011). As nitrogen fixation consumes a lot of energy, its occurrence typically means there is extremely low marine nitrogen content (Luo et al., 2011; Wu et al., 2022). However, upward-migration of chemocline with the marine transgression in the earliest Triassic (Riccardi et al., 2006) may possibly have brought NH_3 with low $\delta^{15}N_{org}$ from the deep ferruginous ocean, and the NH_3 was then oxidized to nitrate in shallow-marine settings (Busigny et al., 2013). This incursion of deep water NH_3 with low $\delta^{15}N_{org}$ would have favored the decreasing $\delta^{15}N_{org}$ and restoration of marine N reservoir after de-oxygenation (Luo et al., 2011; Boyle et al., 2013; Sun et al., 2019).

On the other hand, reduced denitrification may also have contributed to the $\delta^{15}N_{org}$ decrease. If assuming nitrogen is not biolimiting in the earliest Triassic, the P concentration possibly controlled marine primary productivity and shallow-marine redox conditions (Müller et al., 2022). As previously reported, intensified warming and aridification from latest Permian to early Triassic may have led to increasing dominance of physical weathering over chemical weathering on land (cf. Schobben et al., 2020; Xu et al., 2023), possibly reducing continental nutrient fluxes (supported by decreasing P_{tot}/Al). Moreover, oceanic stagnation was promoted by climatic warming (Shen et al., 2015). As a consequence of nutrient-influx reduction from continent and deep water, marine primary productivity likely declined from latest Permian to earliest Triassic, which is in accordance with previous studies based on productivity-sensitive elemental proxies (Shen et al., 2015; Müller et al., 2022) and Cd and N isotopes (Zhang et al., 2018b; Sun et al., 2019) in the South China area. Reduced marine primary productivity may have been closely associated with increasing oxygenation that reduced denitrification and decreased $\delta^{15}N_{org}$. Notably, increasing primary productivity has been suggested during latest Permian to earliest Triassic as the cause of ocean euxinia (Hotinski et al., 2001; Xie et al., 2005; Payne and Finnegan, 2006; Meyer et al., 2008). The increase in primary productivity has been attributed to accelerated hydrological cycles, or to increases in continental weathering and nutrient fluxes under climate warming (Xie et al., 2005; Meyer et al., 2008). The difference in interpretations (increase vs. decrease) about primary productivity and nutrient influx may be controlled by: i) changes of continental weathering (physical vs. chemical weathering) under different climates (e.g., warming & humid vs. warming & arid); and ii) the degree to which influenced by continental weathering and ocean upwelling intensity due to different distance to the nutrient source, which need further clarification.

4.4. Global marine redox and implications for latest Permian mass extinction

4.4.1. Differential redox conditions in Neotethys, Boreal Sea and Panthalassa

Marine redox studies have been widely conducted in the Neotethys, Boreal Sea and Panthalassa, but most focused on specific shallow- or deep-marine settings, with very limited studies focusing on the whole water column. As in the present study, temporal and spatial variation of marine redox conditions from a proximal-to-distal view were investigated for the Neotethys by Clarkson et al. (2016), Panthalassa by Algeo et al. (2011), and the Boreal Ocean by Schobben et al. (2020) (Fig. 7), permitting a comparison and evaluation of global-scale ocean-redox evolution during the P-Tr transition. Remarkably, previous studies in these ocean areas document different proximal-to-distal redox histories during the P-Tr transition.

In the Neotethys Ocean (Oman), Clarkson et al. (2016) used Fe-S-C systematics to explore ocean-redox variation during the P-Tr transition along a shelf-to-basin transect, revealing that: i) in the pre-LPME interval (Upper Permian, *C. changxingensis* Zone), anoxic and ferruginous conditions only appeared intermittently in mid-slope settings but with oxic upper slope and deeper slope-basinal settings; ii) during the LPME

(uppermost Permian, *C. yini* to *C. meishanensis* zones), anoxic and ferruginous conditions expanded from mid-slope to basinal settings, but with oxic upper slope settings; iii) in the post-LPME interval (lowermost Triassic, *H. parvus* to *I. isarcica* zones), oxic conditions covered platform to basinal settings (Fig. 7 A1-A3). The mainly ferruginous conditions around the LPME herein were attributed to the weathering flux of Fe_{HR} exceeding that of sulfate (Clarkson et al., 2016). The P-Tr proximal-to-distal marine redox changes revealed by Clarkson et al. (2016) were in accordance with other P-Tr marine redox studies in the Neotethys from different (shallow or deep) water depths (Garbelli et al., 2016; Eltom et al., 2017; Stebbins et al., 2019; Huang et al., 2019). In contrast, intensified anoxic basinal conditions have been advocated from latest Permian to earliest Triassic in the Hovea 3 core of the Neotethys, an environmental condition that may have been related to local basinal restriction (Grice et al., 2005; Bond and Wignall, 2010; Georgiev et al., 2020, and references therein).

Changes in marine redox conditions in the open Panthalassic Ocean have been analyzed based on lithology, framboidal pyrites and redox-sensitive geochemistry (Isozaki, 1997; Suzuki et al., 1998; Kato et al., 2002; Matsuo et al., 2003; Algeo et al., 2010, 2011; Kaiho et al., 2012; Takahashi et al., 2014; Grasby et al., 2021). Redox conditions during the end-Permian mass extinction have been interpreted as either strongly anoxic (even euxinic) or as suboxic to weakly anoxic, which may be related to different sampling and analytical strategies, while a higher sampling resolution suggests anoxic (even) euxinic conditions (Algeo et al., 2010, 2011; Kaiho et al., 2012; Takahashi et al., 2014; Grasby et al., 2021). Based on previous studies, the secular trend of ocean-redox changes at various water depths is as follows (Fig. 7 B1-B3): i) in the pre-LPME interval (Upper Permian), shallower water areas were characterized by suboxic intermediate and bottomwaters, whereas deeper water areas were characterized by oxic-suboxic intermediate and bottomwaters; ii) during the LPME (uppermost Permian), shallower and deeper water areas were both characterized by anoxic and/or euxinic conditions; and iii) in the post-LPME interval (lowermost Triassic), shallower water areas were characterized by euxinic intermediate and anoxic bottomwaters, whereas deeper water areas were characterized by euxinic intermediate and suboxic bottomwaters.

In the Boreal Sea, Schobben et al. (2020) assessed the proximal-to-distal ocean-redox variations around the LPME (Fig. 7 D1-D3), and reported: i) in the pre-LPME interval (Upper Permian), inner-shelf settings were dysoxic and outer-shelf settings oxic; ii) during the LPME (uppermost Permian), inner-shelf settings experienced euxinia, while outer-shelf settings became dysoxic/ferruginous; and iii) in the post-LPME interval (lowermost Triassic), euxinic conditions expanded from inner-shelf to outer-shelf settings. The spatio-temporal variability of redox conditions was consistent with the other findings based on pyrite framboids, Fe speciation and redox-sensitive elements in the Boreal Sea (e.g., Bond and Wignall, 2010; Mettam et al., 2017). Such redox changes may be linked to changes in continental weathering, which modulated continental influx of iron and sulfate. The relative importance between iron and sulfate influx influenced the development of marine ferruginous vs. euxinic conditions, which further controlled the marine phosphorus cycle and the extension and intensity of marine de-oxygenation (Schobben et al., 2020).

4.4.2. *Possible links between marine redox variation and the Siberian Traps LIP*

Comparison of data from the Neotethys, Paleotethys, Panthalassa and Boreal oceans reveals considerable spatial and temporal variation in marine redox conditions during the P-Tr transition (Fig. 7). Such variation has frequency been linked to regional differences in continental weathering (Algeo et al., 2011; Clarkson et al., 2016; Schobben et al., 2020). For the Neotethys, Clarkson et al. (2016) suggested an enhanced continental flux of Fe_{HR} over sulfate during and after the LPME, promoting the development of ferruginous conditions. Further, Clarkson et al. (2016) proposed that the enhanced Fe_{HR} influx may have been related to increased Fe_{HR} release from parent silicate minerals and higher aeolian Fe flux, which was exacerbated by destabilized soil material with the loss of terrestrial vegetation. For the Boreal Sea, Schobben et al. (2020) proposed increased physical weathering relative to chemical weathering during the latest Permian to earliest Triassic due to climatic warming, and this change may have led to less continental influx of Fe_{HR} and a relative excess of sulfate influx, thereby promoting marine euxinia. However, in the South China, enhanced physical relative to chemical weathering has been reported during the P-Tr transition (Xu et al., 2017), and this weathering change corresponded to a development of ferruginous ocean (Fig. 7).

Changes in continental weathering during the P-Tr transition have frequently been linked to STLIP volcanic activity (Xie et al., 2007; Clarkson et al., 2016; Sun et al., 2018; Liu et al., 2020; Schobben et al., 2020). During the P-Tr transition, as mentioned above, the distance to STLIP decreased from the Neotethys Ocean, to the Paleotethys Ocean, then to the Boreal Sea (Fig. 1A). With increasing proximity to the Siberian Traps LIP (i.e., from the Neotethys to the Boreal Sea), marine de-oxygenation became more intense around the LPME (Figs. 1 and 7). The spatial coupling relationship suggests the possibility that the STLIP acted as a major source of sulfur that led to spatial variation in seawater sulfate concentrations, given the small size of the oceanic sulfate reservoir at that time (Luo et al., 2010; Schobben et al., 2015). This is supported by the occurrence of much lower $\delta^{34}S_{py}$ (ca. –50 to −40‰) in the Boreal Sea (Schobben et al., 2020) than in other oceanic regions during the P-Tr transition (ca. –40 to −20‰; Fig. 4) (Algeo et al., 2010, 2011; Clarkson et al., 2016). The intensity of sulfur release (e.g., via dissolution of sulfur in basaltic magmas, sulfate aerosol emission, intrusion into strata containing abundant anhydrite) during volcanism may have played a significant role in controlling the global extent and intensity of marine de-oxygenation (Maruoka et al., 2003). Volcanic-related sulfur influence is a possible reason for the contradictory interpretation of continental Fe_{HR} and sulfate flux related to P-Tr weathering by Clarkson et al. (2016) and Schobben et al. (2020). In addition, the distance to continents and paleogeographic restriction degree may also have influenced marine Fe and sulfate concentrations as well as redox conditions (Algeo et al., 2010, 2011; Newby et al., 2021). Despite ocean-redox variation, all oceanic regions exhibited a degree of shallow-marine deoxygenation during the LPME, suggesting a possible link between marine deoxygenation and the end-Permian biocrisis. After the LPME, regional differences in redox conditions may partially account for the long and complex process of marine ecosystem recovery during the Early Triassic.

5. Conclusions

This study investigated the extent and magnitude of marine de-oxygenation of the eastern Paleotethys water column (shelf to basin), as recorded in Permian-Triassic boundary sections in South China. The results highlight dynamic marine redox conditions, which varied strongly both spatially and temporally during the P-Tr transition. Basinal settings mainly remained ferruginous conditions from the latest Permian *C. changxingensis* to the earliest Triassic *H. parvus-I. isarcica* zones. In deep middle-shelf to outer-shelf settings, a change in dominance from euxinic (*C. changxingensis* Zone) to ferruginous (*C. yini* to *I. isarcica* zones) conditions coincided with increased P burial (i.e., high P_{tot}/Al) and low $\delta^{15}N_{org}$. In inner shelf and shallower middle-shelf settings, the latest Permian shift from oxic (*C. changxingensis* Zone) to euxinic (*C. yini-C. meishanensis* zones) conditions was accompanied by decreasing P burial (i.e., low P_{tot}/Al), and increasing nitrogen fixation and/or decreasing denitrification (i.e., decreasing $\delta^{15}N_{org}$) by diminished marine productivity. This was followed in the earliest Triassic (*H. parvus-I. isarcica* zones) by a shift to ferruginous-oxic conditions accompanied by increased P burial, incomplete nutrient nitrogen utilization, and/or weak denitrification (i.e., low $\delta^{15}N_{org}$) as well as low marine productivity.

Based on a comparison of the whole-water column redox evolution of marine P-Tr sections in South China with those in the Neotethys, Panthalassic, and Boreal oceans, we infer that the process of de-oxygenation of P-Tr marine environments was strongly influenced by distance to the Siberian Traps LIP and, thus, to the volume of its related sulfur emissions, which resulted in greater volcanic influences on climate, continental weathering, and riverine fluxes in high-latitude Northern Hemisphere oceans than elsewhere. Furthermore, shallow-marine de-oxygenation developed in all four of these oceanic regions during the LPME and, thus, may have played an important role in the marine biocrisis.

Declaration of Competing Interest

The authors declare that they have no known competing financial interests or personal relationships that could have appeared to influence the work reported in this paper.

Data availability

Data will be made available on request.

Acknowledgments

This study is financially supported by National Natural Science Foundation of China (No. 42202123, 41888101, 42272116), Sichuan Provincial Youth Science & Technology Innovative Research Group Fund (No. 2022JDTD0004).

Appendix A. Supplementary data

Supplementary data to this article can be found online at https://doi.org/10.1016/j.earscirev.2023.104576.

References

Algeo, T., Ingall, E., 2007. Sedimentary C_{org}:P ratios, paleocean ventilation, and Phanerozoic atmospheric pO_2. Palaeogeogr. Palaeoclimatol. Palaeoecol. 256, 130–155.

Algeo, T.J., Ellwood, B., Nguyen, T.K.T., Rowe, H., Maynard, J.B., 2007. The Permian–Triassic boundary at Nhi Tao, Vietnam: evidence for recurrent influx of sulfidic watermasses to a shallow-marine carbonate platform. Palaeogeogr. Palaeoclimatol. Palaeoecol. 252, 304–327.

Algeo, T., Shen, Y., Zhang, T., Lyons, T., Bates, S., Rowe, H., Nguyen, T.K.T., 2008. Association of ^{34}S-depleted pyrite layers with negative carbonate δ^{13}C excursions at the Permian-Triassic boundary: evidence for upwelling of sulfidic deep-ocean water masses. Geochem. Geophys. Geosystems 9, Q04025.

Algeo, T.J., Henderson, C.M., Tong, J., Feng, Q., Yin, H., Tyson, R.V., 2013. Plankton and productivity during the Permian–Triassic boundary crisis: an analysis of organic carbon fluxes. Glob. Planet. Change 105, 52–67.

Algeo, T.J., Hinnov, L., Moser, J., Maynard, J.B., Elswick, E., Kuwahara, K., Sano, H., 2010. Changes in productivity and redox conditions in the Panthalassic Ocean during the latest Permian. Geology 38, 187–190.

Algeo, T.J., Kuwahara, K., Sano, H., Bates, S., Lyons, T., Elswick, E., Hinnov, L., Ellwood, B., Moser, J., Maynard, J.B., 2011. Spatial variation in sediment fluxes, redox conditions, and productivity in the Permian–Triassic Panthalassic Ocean. Palaeogeogr. Palaeoclimatol. Palaeoecol. 308, 65–83.

Algeo, T.J., Meyers, P.A., Robinson, R.S., Rowe, H., Jiang, G.Q., 2014. Icehouse–greenhouse variations in marine denitrification. Biogeosciences 11, 1273–1295.

Bond, D.P., Wignall, P.B., 2010. Pyrite framboid study of marine Permian–Triassic boundary sections: a complex anoxic event and its relationship to contemporaneous mass extinction. Geol. Soc. Am. Bull. 122, 1265–1279.

Boyle, R.A., Clark, J.R., Poulton, S.W., Shields-Zhou, G., Canfield, D.E., Lenton, T.M., 2013. Nitrogen cycle feedbacks as a control on euxinia in the mid-Proterozoic ocean. Nat. Commun. 4, 1533.

Brayard, A., Krumenacker, L.J., Botting, J.P., Jenks, J.F., Bylund, K.G., Fara, E., Vennin, E., Olivier, N., Goudemand, N., Saucède, T., Charbonnier, S., 2017. Unexpected Early Triassic marine ecosystem and the rise of the Modern evolutionary fauna. Sci. Adv 3 e1602159.

Brookfield, M.E., Stebbins, A.G., Rampino, M.R., Hannigan, R.E., 2018. Significance of carbon, nitrogen and their isotopic changes in a Permian-Triassic non-marine boundary section at Carlton Heights (Karoo Basin), South Africa. J. Afr. Earth Sci. 145, 170–177.

Busigny, V., Lebeau, O., Ader, M., Krapež, B., Bekker, A., 2013. Nitrogen cycle in the Late Archean ferruginous ocean. Chem. Geol. 362, 115–130.

Calvert, S.E., Nielsen, B., Fontugne, M.R., 1992. Evidence from nitrogen isotope ratios for enhanced productivity during formation of eastern Mediterranean sapropels. Nature 359, 223–225.

Chen, Z., Algeo, T.J., Bottjer, D.J., 2014. Global review of the Permian-Triassic mass extinction and subsequent recovery: Part I. Earth Sci. Rev. 137, 1–5.

Clarkson, M.O., Poulton, S.W., Guilbaud, R., Wood, R.A., 2014. Assessing the utility of Fe/Al and Fe-speciation to record water column redox conditions in carbonate-rich sediments. Chem. Geol. 382, 111–122.

Clarkson, M.O., Wood, R.A., Poulton, S.W., Richoz, S., Newton, R.J., Kasemann, S.A., Bowyer, F., Krystyn, L., 2016. Dynamic anoxic ferruginous conditions during the end-Permian mass extinction and recovery. Nat. Commun. 7, 12236.

Eltom, H.A., Abdullatif, O.M., Babalola, L.O., 2017. Redox conditions through the Permian-Triassic transition in the upper Khuff formation, Saudi Arabia. Palaeogeogr. Palaeoclimatol. Palaeoecol. 472, 203–215.

Eroglu, S., Scholz, F., Salvatteci, R., Siebert, C., Schneider, R., Frank, M., 2021. The impact of postdepositional alteration on iron-and molybdenum-based redox proxies. Geology 49, 1411–1415.

Erwin, D.H., Bowring, S.A., Yugan, J., Koeberl, C., MacLeod, K.G., 2002. End-Permian mass extinctions: a review. Geol. Soc. Am. Spec. Paper 356, 363–384.

Garbelli, C., Angiolini, L., Brand, U., Shen, S.Z., Jadoul, F., Posenato, R., Azmy, K., Cao, C.Q., 2016. Neotethys seawater chemistry and temperature at the dawn of the end Permian mass extinction. Gondwana Res 35, 272–285.

Ge, Y., Bond, D.P., 2022. Two deep marine oxygenation events during the Permian-Triassic boundary interval in South China: relationship with ocean circulation and marine primary productivity. Earth Sci. Rev 234, 104220.

Georgiev, S.V., Stein, H.J., Yang, G., Hannah, J.L., Böttcher, M.E., Grice, K., Holman, A.I., Turgeon, S., Simonsen, S., Cloquet, C., 2020. Late Permian–early Triassic environmental changes recorded by multi-isotope (Re-Os-N-Hg) data and trace metal distribution from the Hovea-3 section, Western Australia. Gondwana Res. 88, 353–372.

Grasby, S.E., Beauchamp, B., Embry, A., Sanei, H., 2013. Recurrent early Triassic Ocean anoxia. Geology 41, 175–178.

Grasby, S.E., Bond, D.P.G., Wignall, P.B., Yin, R., Strachan, L.J., Takahashi, S., 2021. Transient Permian-Triassic euxinia in the southern Panthalassa deep ocean. Geology 49, 889–893.

Grice, K., Cao, C., Love, G.D., Böttcher, M.E., Twitchett, R.J., Grosjean, E., Summons, R. E., Turgeon, S.C., Dunning, W., Jin, Y., 2005. Photic zone euxinia during the Permian-Triassic superanoxic event. Science 307, 706–709.

Gruber, N.G., 2008. The marine nitrogen cycle: overview and challenges. In: Capone, D. G., Bronk, D.A., Mulholland, M.R., Carpenter, E.J. (Eds.), Nitrogen in the Marine Environment, 2nd edn. Elsevier, Amsterdam, pp. 1–50.

He, L., Wang, Y., Woods, A., Li, G., Yang, H., Liao, W., 2013. An oxygenation event occurred in deep shelf settings immediately after the end-Permian mass extinction in South China. Glob. Planet. Change 101, 72–81.

Hotinski, R.M., Bice, K.L., Kump, L.R., Najjar, R.G., Arthur, M.A., 2001. Ocean stagnation and end-Permian anoxia. Geology 29, 7–10.

Huang, Y., Chen, Z.Q., Algeo, T.J., Zhao, L., Baud, A., Bhat, G.M., Zhang, L., Guo, Z., 2019. Two-stage marine anoxia and biotic response during the Permian–Triassic transition in Kashmir, northern India: pyrite framboid evidence. Glob. Planet. Change 172, 124–139.

Isozaki, Y., 1997. Permo-Triassic boundary superanoxia and stratified superocean: records from lost deep sea. Science 276, 235–238.

Jiang, H., Lai, X., Luo, G., Aldridge, R., Zhang, K., Wignall, P., 2007. Restudy of conodont zonation and evolution across the P/T boundary at Meishan section, Changxing, Zhejiang, China. Glob. Planet. Change 55, 39–55.

Jin, Y.G., Wang, Y., Wang, W., Shang, Q.H., Cao, C.Q., Erwin, D.H., 2000. Pattern of marine mass extinction near the Permian-Triassic boundary in South China. Science 289, 432–436.

Kaiho, K., Kajiwara, Y., Chen, Z.Q., Gorjan, P., 2006. A sulfur isotope event at the end of the Permian. Chem. Geol. 235, 33–47.

Kaiho, K., Oba, M., Fukuda, Y., Ito, K., Ariyoshi, S., Gorjan, P., Riu, Y., Takahashi, S., Chen, Z.Q., Tong, J., Yamakita, S., 2012. Changes in depth-transect redox conditions spanning the end-Permian mass extinction and their impact on the marine extinction: evidence from biomarkers and sulfur isotopes. Glob. Planet. Change 94, 20–32.

Kamo, S.L., Czamanske, G.K., Amelin, Y., Fedorenko, V.A., Davis, D.W., Trofimov, V.R., 2003. Rapid eruption of Siberian flood-volcanic rocks and evidence for coincidence with the Permian–Triassic boundary and mass extinction at 251 Ma. Earth Planet. Sci. Lett. 214, 75–91.

Kato, Y., Nakao, K., Isozaki, Y., 2002. Geochemistry of Late Permian to Early Triassic pelagic cherts from southwest Japan: implications for an oceanic redox change. Chem. Geol. 182, 15–34.

Kump, L.R., Pavlov, A., Arthur, M.A., 2005. Massive release of hydrogen sulfide to the surface ocean and atmosphere during intervals of oceanic anoxia. Geology 33, 397–400.

Lau, K.V., Maher, K., Altiner, D., Kelley, B.M., Kump, L.R., Lehrmann, D.J., Silva-Tamayo, J.C., Weaver, K.L., Yu, M., Payne, J.L., 2016. Marine anoxia and delayed Earth system recovery after the end-Permian extinction. Proc. Natl. Acad. Sci. U. S. A. 113, 2360–2365.

Lei, Y., Servais, T., Feng, Q., He, W., 2012. The spatial (nearshore–offshore) distribution of latest Permian phytoplankton from the Yangtze Block, South China. Palaeogeogr. Palaeoclimatol. Palaeoecol. 363, 151–162.

Lei, L.D., Shen, J., Li, C., Algeo, T.J., Chen, Z.Q., Feng, Q.L., Cheng, M., Jin, C.S., Huang, J.H., 2017. Controls on regional marine redox evolution during Permian-

Triassic transition in South China. Palaeogeogr. Palaeoclimatol. Palaeoecol. 486, 17–32.
Li, G., Wang, Y., Li, S., Wang, T., Liao, W., Deng, B., Lai, Z., 2022. Biotic response to rapid environmental changes during the Permian–Triassic mass extinction. Front. Mar. Sci. 9, 911492.
Li, G., Wang, Y., Shi, G.R., Liao, W., Yu, L., 2016. Fluctuations of redox conditions across the Permian–Triassic boundary—new evidence from the GSSP section in Meishan of South China. Palaeogeogr. Palaeoclimatol. Palaeoecol. 448, 48–58.
Liu, Z., Selby, D., Zhang, H., Shen, S., 2020. Evidence for volcanism and weathering during the Permian-Triassic mass extinction from Meishan (South China) osmium isotope record. Palaeogeogr. Palaeoclimatol. Palaeoecol. 553, 109790.
Luo, G., Kump, L.R., Wang, Y., Tong, J., Arthur, M.A., Yang, H., Huang, J., Yin, H., Xie, S., 2010. Isotopic evidence for an anomalously low oceanic sulfate concentration following end-Permian mass extinction. Earth Planet. Sci. Lett. 300, 101–111.
Luo, G., Wang, Y., Algeo, T.J., Kump, L.R., Bai, X., Yang, H., Yao, L., Xie, S., 2011. Enhanced nitrogen fixation in the immediate aftermath of the latest Permian marine mass extinction. Geology 39, 647–650.
Maruoka, T., Koeberl, C., Hancox, P.J., Reimold, W.U., 2003. Sulfur geochemistry across a terrestrial Permian–Triassic boundary section in the Karoo Basin, South Africa. Earth Planet. Sci. Lett. 206, 101–117.
Matsuo, M., Kubo, K., Isozaki, Y., 2003. Mössbauer spectroscopic study on characterization of iron in the Permian to Triassic deep-sea chert from Japan. Hyperfine Interact. 5, 435–438.
Mettam, C., Zerkle, A.L., Claire, M.W., Izon, G., Junium, C.J., Twitchett, R.J., 2017. High-frequency fluctuations in redox conditions during the latest Permian mass extinction. Palaeogeogr. Palaeoclimatol. Palaeoecol. 485, 210–223.
Meyer, K.M., Kump, L.R., Ridgwell, A., 2008. Biogeochemical controls on photic-zone euxinia during the end-Permian mass extinction. Geology 36, 747–750.
Müller, J., Sun, Y., Yang, F., Fantasia, A., Joachimski, M., 2022. Phosphorus cycle and primary productivity changes in the Tethys Ocean during the Permian-Triassic transition: Starving marine ecosystems. Front. Earth Sci. 10, 832308.
Newby, S.M., Owens, J.D., Schoepfer, S.D., Algeo, T.J., 2021. Transient ocean oxygenation at end-Permian mass extinction onset shown by thallium isotopes. Nat. Geosci. 14, 678–683.
Newton, R.J., Bond, D., Cope, H., Wignall, P.B., 2009. A framboid gap at the Permo-Triassic boundary. Geochimica et Cosmochimica Acta Supplement 73, A939.
Newton, R.J., Pevitt, E.L., Wignall, P.B., Bottrell, S.H., 2004. Large shifts in the isotopic composition of seawater sulphate across the Permo–Triassic boundary in northern Italy. Earth Planet. Sci. Lett. 218, 331–345.
Payne, J.L., Finnegan, S., 2006. Controls on marine animal biomass through geological time. Geobiology 4, 1–10.
Pietsch, C., Bottjer, D.J., 2014. The importance of oxygen for the disparate recovery patterns of the benthic macrofauna in the Early Triassic. Earth Sci. Rev. 137, 65–84.
Poulton, S.W., Canfield, D.E., 2011. Ferruginous conditions: a dominant feature of the ocean through earth's history. Element 7, 486–490.
Reichow, M.K., Pringle, M.S., Al'Mukhamedov, A.I., Allen, M.B., Andreichev, V.L., Buslov, M.M., Davies, C.E., Fedoseev, G.S., Fitton, J.G., Inger, S., Medvedev, A.Y., 2009. The timing and extent of the eruption of the Siberian Traps large igneous province: implications for the end-Permian environmental crisis. Earth Planet. Sci. Lett. 277, 9–20.
Renne, P.R., Black, M.T., Zichao, Z., Richards, M.A., Basu, A.R., 1995. Synchrony and causal relations between Permian-Triassic boundary crises and Siberian flood volcanism. Science 269, 1413–1416.
Riccardi, A.L., Arthur, M.A., Kump, L.R., 2006. Sulfur isotopic evidence for chemocline upward excursions during the end-Permian mass extinction. Geochim. Cosmochim. Acta 70, 5740–5752.
Robinson, R.S., Kienast, M., Luiza Albuquerque, A., Altabet, M., Contreras, S., De Pol Holz, R., Dubois, N., Francois, R., Galbraith, E., Hsu, T.C., Ivanochko, T., 2012. A review of nitrogen isotopic alteration in marine sediments. Paleoceanography 27, PA4203.
Ruttenberg, K.C., Ogawa, N.O., Tamburini, F., Briggs, R.A., Colasacco, N.D., Joyce, E., 2009. Improved, high-throughput approach for phosphorus speciation in natural sediments via the SEDEX sequential extraction method. Limnol. Oceanogr. 7, 319–333.
Saitoh, M., Ueno, Y., Isozaki, Y., Yoshida, N., 2021. Multiple sulfur isotope chemostratigraphy across the Permian-Triassic boundary at Chaotian, China: implications for a shoaling model of toxic deep-waters. Island Arc 30, e12398.
Schobben, M., Foster, W.J., Sleveland, A., Zuchuat, V., Svensen, H.H., Planke, S., Bond, D.P., Marcelis, F., Newton, R.J., Wignall, P.B., Poulton, S.W., 2020. A nutrient control on marine anoxia during the end-Permian mass extinction. Nat. Geosci. 13, 640–646.
Schobben, M., Stebbins, A., Ghaderi, A., Strauss, H., Korn, D., Korte, C., 2015. Flourishing ocean drives the end-Permian marine mass extinction. Proc. Natl. Acad. Sci. U.S.A. 112, 10298–10303.
Scotese, C.R., Langford, R.P., 1995. Pangea and the paleogeography of the Permian. In: Scholle, A., Peryt, T.M., Ulmer-Scholle, D.A. (Eds.), The Permian of Northern Pangea, vol. 1. Springer, Berlin, pp. 3–19.
Shen, Y., Farquhar, J., Zhang, H., Masterson, A., Zhang, T., Wing, B.A., 2011. Multiple S-isotopic evidence for episodic shoaling of anoxic water during late Permian mass extinction. Nat. Commun. 2, 210.
Shen, S.Z., Ramezani, J., Chen, J., Cao, C.Q., Erwin, D.H., Zhang, H., Xiang, L., Schoepfer, S.D., Henderson, C.M., Zheng, Q.F., Bowring, S.A., 2019. A sudden end-Permian mass extinction in South China. Geol. Soc. Am. Bull. 131, 205–223.
Shen, J., Schoepfer, S.D., Feng, Q., Zhou, L., Yu, J., Song, H.Y., Wei, H., Algeo, T.J., 2015. Marine productivity changes during the end-Permian crisis and early Triassic recovery. Earth Sci. Rev. 149, 136–162.
Sigman, D.M., Casciotti, K.L., 2001. Nitrogen isotopes in the ocean. Encyclopedia of Ocean Sciences 3, 1884–1894.
Smith, R.M., Ward, P.D., 2001. Pattern of vertebrate extinctions across an event bed at the Permian-Triassic boundary in the Karoo Basin of South Africa. Geology 29, 1147–1150.
Son, T.H., Koeberl, C., Ngoc, N.L., Huyen, D.T., 2007. The Permian-Triassic boundary sections in northern Vietnam (Nhi Tao and Lung Cam sections): Carbon-isotope excursion and elemental variations indicate major anoxic event. Palaeoworld 16, 51–66.
Song, H., Tong, J., Algeo, T.J., Horacek, M., Qiu, H., Song, H., Tian, L., Chen, Z.Q., 2013a. Large vertical δ13CDIC gradients in early Triassic seas of the South China craton: Implications for oceanographic changes related to Siberian Traps volcanism. Global Planet. Change 105, 7–20.
Song, H.J., Wignall, P.B., Tong, J., Yin, H., 2013b. Two pulses of extinction during the Permian–Triassic crisis. Nat. Geosci. 6, 52–56.
Song, H.J., Wignall, P.B., Dunhill, A.M., 2018. Decoupled taxonomic and ecological recoveries from the Permo-Triassic extinction. Sci. Adv 4 eaat5091.
Stebbins, A., Williams, J., Brookfield, M., Nye Jr., S.W., Hannigan, R., 2019. Frequent euxinia in southern Neo-Tethys Ocean prior to the end-Permian biocrisis: evidence from the Spiti region, India. Palaeogeogr. Palaeoclimatol. Palaeoecol. 516, 1–10.
Summons, R.E., Love, G.D., Hays, L., Cao, C., Jin, Y., Shen, S.Z., Grice, K., Foster, C.B., 2006. Molecular evidence for prolonged photic zone euxinia at the Meishan and East Greenland sections of the Permian Triassic Boundary. Geochim. Cosmochim. Acta 70, A625.
Sun, D., Tong, J., Xiong, Y., Tian, L., Yin, H., 2012. Conodont biostratigraphy and evolution across Permian-Triassic boundary at Yangou section, Leping, Jiangxi Province, South China. J. Earth Sci. 23, 311–325.
Sun, H., Xiao, Y., Gao, Y., Zhang, G., Casey, J.F., Shen, Y., 2018. Rapid enhancement of chemical weathering recorded by extremely light seawater lithium isotopes at the Permian–Triassic boundary. Proc. Natl. Acad. Sci. U. S. A. 115, 3782–3787.
Sun, Y.D., Zulla, M.J., Joachimski, M.M., Bond, D.P.G., Wignall, P.B., Zhang, Z.T., Zhang, M.H., 2019. Ammonium ocean following the end-Permian mass extinction. Earth Planet. Sci. Lett. 518, 211–222.
Suzuki, N., Ishida, K., Shinomiya, Y., Ishiga, H., 1998. High productivity in the earliest Triassic Ocean: black shales, Southwest Japan. Palaeogeogr. Palaeoclimatol. Palaeoecol. 141, 53–65.
Takahashi, S., Yamasaki, S.I., Ogawa, Y., Kimura, K., Kaiho, K., Yoshida, T., Tsuchiya, N., 2014. Bioessential element-depleted ocean following the euxinic maximum of the end-Permian mass extinction. Earth Planet. Sci. Lett. 393, 94–104.
Tian, L., Tong, J., Xiao, Y., Benton, M.J., Song, H., Song, H., Liang, L., Wu, K., Chu, D., Algeo, T.J., 2019. Environmental instability prior to end-Permian mass extinction reflected in biotic and facies changes on shallow carbonate platforms of the Nanpanjiang Basin (South China). Palaeogeogr. Palaeoclimatol. Palaeoecol. 519, 23–36.
Wang, Y., Jin, Y., 2000. Permian palaeogeographic evolution of the Jiangnan Basin, South China. Palaeogeogr. Palaeoclimatol. Palaeoecol. 160, 35–44.
Wei, H., Algeo, T.J., Yu, H., Wang, J., Guo, C., Shi, G., 2015. Episodic euxinia in the Changhsingian (late Permian) of South China: evidence from framboidal pyrite and geochemical data. Sediment. Geol. 319, 78–97.
Wignall, P.B., Hallam, A., Xulong, L., Fengqing, Y., 1995. Palaeoenvironmental changes across the Permian/Triassic boundary at Shangsi (N. Sichuan, China). Hist Biol 10, 175–189.
Wignall, P.B., Newton, R., 1998. Pyrite framboid diameter as a measure of oxygen deficiency in ancient mudrocks. Am. J. Sci. 298, 537–552.
Wignall, P.B., Twitchett, R.J., 1996. Oceanic anoxia and the end Permian mass extinction. Science 272, 1155–1158.
Wilkin, R.T., Barnes, H.L., 1997. Formation processes of framboidal pyrite. Geochim. Cosmochim. Acta 61, 323–339.
Wilkin, R.T., Barnes, H.L., Brantley, S.L., 1996. The size distribution of framboidal pyrite in modern sediments: an indicator of redox conditions. Geochim. Cosmochim. Acta 60, 3897–3912.
Wu, B., Luo, G., Joachimski, M.M., Wignall, P.B., Lei, L., Huang, J., Lai, X., 2022. Carbon and nitrogen isotope evidence for widespread presence of anoxic intermediate waters before and during the Permian-Triassic mass extinction. Geol. Soc. Am. Bull 134, 1397–1413.
Xiang, L., Schoepfer, S.D., Zhang, H., Yuan, D., Cao, C., Zheng, Q., Henderson, C.M., Shen, S., 2016. Oceanic redox evolution across the end-Permian mass extinction at Shangsi, South China. Palaeogeogr. Palaeoclimatol. Palaeoecol. 448, 59–71.
Xiang, L., Zhang, H., Schoepfer, S.D., Cao, C.Q., Zheng, Q.F., Yuan, D.X., Cai, Y.F., Shen, S.Z., 2020. Oceanic redox evolution around the end-Permian mass extinction at Meishan, South China. Palaeogeogr. Palaeoclimatol. Palaeoecol. 544, 109626.
Xiang, L., Schoepfer, S.D., Yuan, D.X., Zheng, Q., Zhang, H., 2022. Oceanic redox evolution across the end-Permian mass extinction at Penglaitan section, South China. Palaeoworld 31, 93–102.
Xiao, Y., Suzuki, N., He, W., 2017. Water depths of the latest Permian (Changhsingian) radiolarians estimated from correspondence analysis. Earth Sci. Rev. 173, 141–158.
Xiao, Y., Wu, K., Tian, L., Benton, M.J., Du, Y., Yang, H., Tong, J., 2018. Framboidal pyrite evidence for persistent low oxygen levels in shallow-marine facies of the Nanpanjiang Basin during the Permian-Triassic transition. Palaeogeogr. Palaeoclimatol. Palaeoecol. 511, 243–255.
Xie, S., Pancost, R.D., Yin, H., Wang, H., Evershed, R.P., 2005. Two episodes of microbial change coupled with Permo/Triassic faunal mass extinction. Nature 434, 494–497.

Xie, S., Pancost, R.D., Huang, J., Wignall, P.B., Yu, J., Tang, X., Chen, L., Huang, X., Lai, X., 2007. Changes in the global carbon cycle occurred as two episodes during the Permian-Triassic crisis. Geology 35, 1083–1086.

Xu, G., Deconinck, J.F., Feng, Q., Baudin, F., Pellenard, P., Shen, J., Bruneau, L., 2017. Clay mineralogical characteristics at the Permian–Triassic Shangsi section and their paleoenvironmental and/or paleoclimatic significance. Palaeogeogr. Palaeoclimatol. Palaeoecol. 474, 152–163.

Xu, G., Shen, J., Algeo, T.J., Yu, J., Feng, Q., Frank, T.D., Fielding, C.R., Yan, J., Deconink, J.F., Lei, Y., 2023. Limited change in silicate chemical weathering intensity during the Permian–Triassic transition indicates ineffective climate regulation by weathering feedbacks. Earth Planet. Sci. Lett 616, 118235.

Yin, H., Jiang, H., Xia, W., Feng, Q., Zhang, N., Shen, J., 2014. The end-Permian regression in South China and its implication on mass extinction. Earth Sci. Rev. 137, 19–33.

Zhang, N., Jiang, H., Zhou, W., Huang, H., Xia, W., 2014. Conodont biostratigraphy across the Permian-Triassic boundary at the Xinmin section, Guizhou, South China. J. Earth Sci. 25, 779–786.

Zhang, F., Algeo, T.J., Romaniello, S.J., Cui, Y., Zhao, L., Chen, Z.Q., Anbar, A.D., 2018a. Congruent Permian-Triassic $\delta^{238}U$ records at Panthalassic and Tethyan sites: Confirmation of global-oceanic anoxia and validation of the U-isotope paleoredox proxy. Geology 46, 327–330.

Zhang, Y., Wen, H., Zhu, C., Fan, H., Cloquet, C., 2018b. Cadmium isotopic evidence for the evolution of marine primary productivity and the biological extinction event during the Permian-Triassic crisis from the Meishan section, South China. Chem. Geol. 481, 110–118.

Zhang, F., Shen, S.Z., Cui, Y., Lenton, T.M., Dahl, T.W., Zhang, H., Zheng, Q.F., Wang, W., Krainer, K., Anbar, A.D., 2020. Two distinct episodes of marine anoxia during the Permian-Triassic crisis evidenced by uranium isotopes in marine dolostones. Geochim. Cosmochim. Acta 287, 165–179.